nature communications

Article

https://doi.org/10.1038/s41467-025-60002-1

Structural basis of transfer RNA processing by bacterial minimal RNase P

Received: 28 September 2023

Accepted: 9 May 2025

Takamasa Teramoto[1,10], Takeshi Koyasu[1,10], Takashi Yokogawa[2,3,4], Naruhiko Adachi[5,9], Kouta Mayanagi[6], Takahiro Nakamura[7], Toshiya Senda[5,8] & Yoshimitsu Kakuta[1]

Precursor tRNAs (pre-tRNAs) require nucleolytic removal of 5′-leader and 3′-trailer sequences for maturation, which is essential for proper tRNA function. The endoribonuclease RNase P exists in diverse forms, including RNA- and protein-based RNase P, and removes 5′-leader sequences from pre-tRNAs. Some bacteria and archaea possess a unique minimal protein-based RNase P enzyme, HARP, which forms dodecamers with twelve active sites. Here, we present cryogenic electron microscopy structures of HARP dodecamers complexed with five pre-tRNAs, and we show that HARP oligomerization enables specific recognition of the invariant distance between the acceptor stem 5′-end and the TψC-loop, functioning as a molecular ruler—a feature representing convergent evolution among RNase P enzymes. The HARP dodecamer uses only five active sites for 5′-leader cleavage, while we identify a 3′-trailer cleavage activity in the remaining seven sites. This elucidation reveals how small proteins evolve through oligomerization to adapt a pivotal biological function (5′-leader processing) and acquire a novel function (3′-trailer processing).

Transfer RNAs (tRNAs) are an essential component of the protein synthesis machinery in all organisms. They play a crucial role in the translation of the genetic code by delivering specific amino acids to ribosomes in a codon-specific manner. Maturation of tRNA from its precursor form is necessary for proper tRNA functionality[1–5]. The 5′-maturation makes charging of tRNAs and interaction with translation factors and the ribosome efficient. Proper maturation is ensured by a group of enzymes known as tRNA-processing enzymes that catalyze a series of cleavage reactions[6], chemical modifications[7–13], and splicing[14–16] of precursor tRNA molecules (pre-tRNAs)[17,18].

In the early steps of tRNA maturation, the endoribonuclease RNase P removes extra 5′ nucleotides (termed 5′-leader) from pre-tRNAs. RNase P is found universally in all three domains of life. Despite the importance of RNase P activity in organisms, its forms are highly diverse. Two fundamentally different forms are known: RNA-based RNase P[19] and protein-based RNase P[20]. RNA-based RNase P enzymes function as ribonucleoprotein (RNP) complexes and are found in

---

[1]Laboratory of Biophysical Chemistry, Department of Bioscience and Biotechnology, Faculty of Agriculture, Kyushu University, 744 Moto-oka, Nishi-ku, Fukuoka 819-0395, Japan. [2]Faculty of Engineering, Gifu University, 1-1 Yanagido, Gifu 501-1193, Japan. [3]United Graduate School of Drug Discovery and Medical Information Sciences, Gifu University, Gifu 501-1193, Japan. [4]Center for One Medicine Innovative Translational Research (COMIT), Institute for Advanced Study, Gifu University, Gifu, Japan. [5]Structural Biology Research Center, Institute of Materials Structure Science, High Energy Accelerator Research Organization (KEK), 1-1 Oho, Tsukuba, Ibaraki 305-0801, Japan. [6]Department of Drug Discovery Structural Biology, Faculty of Pharmaceutical Sciences, Kyushu University, 3-1-1 Maidashi Higashi-ku, Fukuoka 812-8582, Japan. [7]Laboratory of Genome Chemistry and Engineering, Department of Bioscience and Biotechnology, Faculty of Agriculture, Kyushu University, 744 Moto-oka, Nishi-ku, Fukuoka 819-0395, Japan. [8]Department of Materials Structure Science, The Graduate University for Advanced Studies (SOKENDAI), 1-1 Oho, Tsukuba, Ibaraki 305-0801, Japan. [9]Present address: Life Science Center for Survival Dynamics, Tsukuba Advanced Research Alliance (TARA), University of Tsukuba, 1-1-1 Tennodai, Tsukuba, Ibaraki 305-8577, Japan. [10]These authors contributed equally: Takamasa Teramoto, Takeshi Koyasu. e-mail: teramotot@agr.kyushu-u.ac.jp; kakuta@agr.kyushu-u.ac.jp

bacteria, archaea, and eukaryotes. RNA-based RNase P enzymes contain a single catalytic RNA component; however, the number of auxiliary protein components varies depending on the domains of life[21–24]. Since the discovery of RNA-based RNase P almost 40 years ago[25], numerous biochemical and structural studies have elucidated its reaction mechanism[19,21–24,26–33]. The RNA component recognizes the tRNA-specific elbow region formed by the D- and TψC-arms and cleaves off the 5′-leader nucleotides of the pre-tRNA. Two metal ions are required for the 5′-leader processing.

Several protein-based RNase P enzymes have been discovered over the last two decades and are classified into two types[34–36]. The first type, found in eukaryotes, is referred to as protein-only RNase P (PRORP)[37]. PRORP enzymes are approximately 60 kDa proteins composed of three domains: pentatricopeptide repeat (PPR), central, and nuclease domains. Metazoan PRORPs require two additional proteins for catalytic activity[34], whereas plant and *Trypanosoma* PRORPs do not require additional subunits and are self-sufficient for their catalytic activity[35,38]. The second type, HARPs, found in bacteria and archaea, are minimized protein-based RNase P enzymes (~ 23 kDa per monomer). They were first discovered in the hyperthermophilic bacterium *Aquifex aeolicus*[36]. HARPs are comprised of a nuclease domain and a helical domain termed protruding helical (PrH)[39] or spike helix (SH)[40] domain. HARP represents the Homologs of Aquifex RNase P[36] or Hexagram-like assembly proteinaceous RNase P[39].

Structural analyses have revealed information regarding the reaction mechanism of eukaryotic PRORP[41–48]. Recently, the cryogenic electron microscopy (cryo-EM) structure of substrate-bound human PRORP was reported[47]. As with RNA-based RNase P enzymes, PRORPs recognize the elbow region of the bound pre-tRNA and are proposed to employ a two-metal-dependent mechanism for the 5′-leader processing[20]. In contrast, because HARPs are the most recently discovered RNase P enzymes[36], only a limited number of studies on their structures have been reported[39,40]. Cryo-EM structures revealed that HARPs adopt a hexagram-like dodecamer structure that fundamentally differs from the structure of eukaryotic PRORPs[39,40]. Biochemical analysis demonstrated that oligomeric states from tetrameric to dodecameric are essential for the 5′-leader processing of HARPs[40,49,50]. A recent study determined the crystal structure of a non-productive HARP tetramer complexed with one pre-tRNA, revealing that the PrH domain recognizes the pre-tRNA elbow region[50]. These structural analyses suggested that two adjacent dimers cooperate to process a single pre-tRNA substrate. Although previous studies have demonstrated a recognition mechanism for the elbow region of pre-tRNAs, the complete mode of substrate recognition in the HARP dodecamer and the significance of oligomerization remained elusive. Further structural analyses of the HARP dodecamer-pre-tRNA complex are required to fully understand the mechanism of pre-RNA processing.

Here, we show the cryo-EM structures of *Aquifex aeolicus* HARP (*Aa*HARP) and *Hydrogenobacter thermophilus* HARP (*Ht*HARP) dodecamers in complex with pre-tRNA derivatives at an overall resolution of 2.87 Å and 3.19 Å, respectively. Structural and mutational analyses reveal the tRNA-binding mode of HARPs. In addition, biochemical assays demonstrate the capability of HARP to cleave 3′-trailer sequences of pre-tRNAs. This study suggests that HARPs utilize five active sites in the HARP dodecamer for 5′-leader processing and some of the seven vacant active sites for 3′-trailer processing, indicating that HARPs acquired bifunctional activity via oligomerization. In addition, we provide structural insights into the significance of HARP oligomerization. This study provides the missing link necessary for the complete picture of RNase P enzymes and a framework for deciphering tRNA maturation mechanisms.

Results

Cryo-EM structures of HARP:pre-tRNA complexes

To understand the pre-tRNA processing mechanism of HARP enzymes, we determined the structures of *Aa*HARP and *Ht*HARP in complexes with pre-tRNA using cryo-EM single particle analysis with overall resolutions of 2.87 Å and 3.19 Å, respectively (Supplementary Figs. 1–4 and Supplementary Table 1). Using the engineered protein (Supplementary Fig. 5) and the phosphorothioate-modified *A. aeolicus* pre-tRNA^{Val} substrate that contained a 4-nt long 5′-leader (Supplementary Fig. 6), we successfully formed a stable complex between *Aa*HARP and the pre-tRNA derivatives. The protein-substrate complex was prepared by incubating the enzyme with a two-fold excess of the pre-tRNA in the presence of 5 mM Mg^{2+}. During cryo-EM reconstitution of *Ht*HARP, we observed cryo-EM potential maps at some active sites that may represent metal ions. (Supplementary Figs. 4g and 7).

The reconstitutions showed an overall radial architecture, and potential maps corresponding to the five pre-tRNA molecules were observed (Fig. 1). The HARP protomer assembled into a dimer via the PrH domain. The six dimers (A1/A2–F1/F2) assembled into a dodecamer with a left-handed one-turn superhelical structure (Fig. 1). We chose to refer to the five bound pre-tRNA molecules as T1–T5 molecules. The overall structures of the *Aa*HARP and *Ht*HARP dodecamers were identical (root-mean-square distance, RMSD = 2.11 Å over 1794 Cα atoms; Supplementary Fig. 8). Moreover, the overall structure of the pre-tRNA-bound *Aa*HARP was almost identical to that of the previously determined pre-tRNA-free *Aa*HARP[39] (RMSD = 1.32 Å over 2203 Cα atoms) (Supplementary Figs. 9, 10a).

HARP dodecamer-five pre-tRNAs binding

We determined the cryo-EM structure of a productive HARP dodecamer in complex with five pre-tRNAs (Fig. 1 and Supplementary Movie 1). The pre-tRNA molecules alternately bound to the upper and lower layer of the distorted two-layer HARP dodecamer, resulting in five pre-tRNA-binding sites (Fig. 1, top left). These five pre-tRNA-bound structures were distinct from the ten pre-tRNA-bound structures predicted in previous studies[39,40]. The prediction models suggested that the two-layer structure could bind up to five pre-tRNAs in both the upper and lower layers (a total of ten pre-tRNAs; Supplementary Fig. 10b). The cryo-EM structure presented here revealed that the pre-tRNAs are bound with a 15° tilt compared with previous predictions (Supplementary Fig. 10b), resulting in the inability of the pre-tRNA to bind to the upper and lower layers simultaneously, owing to steric hindrance.

For the structures of the HARP:pre-tRNA complexes, we classified the constitutive dimers of the dodecamer into recognition dimers (green) and catalytic dimers (blue; Fig. 1 and Supplementary Fig. 8). The recognition and catalytic dimers alternate in the dodecameric assembly (Fig. 1), and have identical structures (RMSD = 0.35 Å over 340 Cα atoms). Constitutive dimers can either function as recognition or catalytic dimers depending on the binding mode of the pre-tRNA (details in Supplementary Fig. 11). The recognition dimer is exclusively involved in the recognition of pre-tRNAs, and their proposed active sites are unoccupied by the 5′-region around the cleavage site of pre-tRNAs. In contrast, the catalytic dimers are responsible for HARP catalysis. The 5′-regions of adjacent pre-tRNAs occupy the active sites in the catalytic dimer. In addition, the catalytic dimers contact the acceptor stems of the bound pre-tRNAs. In this study, the HARP dodecamers contained three recognition dimers (B1/B2, D1/D2, and F1/F2; Fig. 1) and three catalytic dimers (A1/A2, C1/C2, and E1/E2; Fig. 1). For instance, the C1/C2 dimer catalyzes 5′-leader processing of pre-tRNAs T2 and T3. The D1/D2 dimer recognizes the elbow regions of pre-tRNAs T3 and T4.

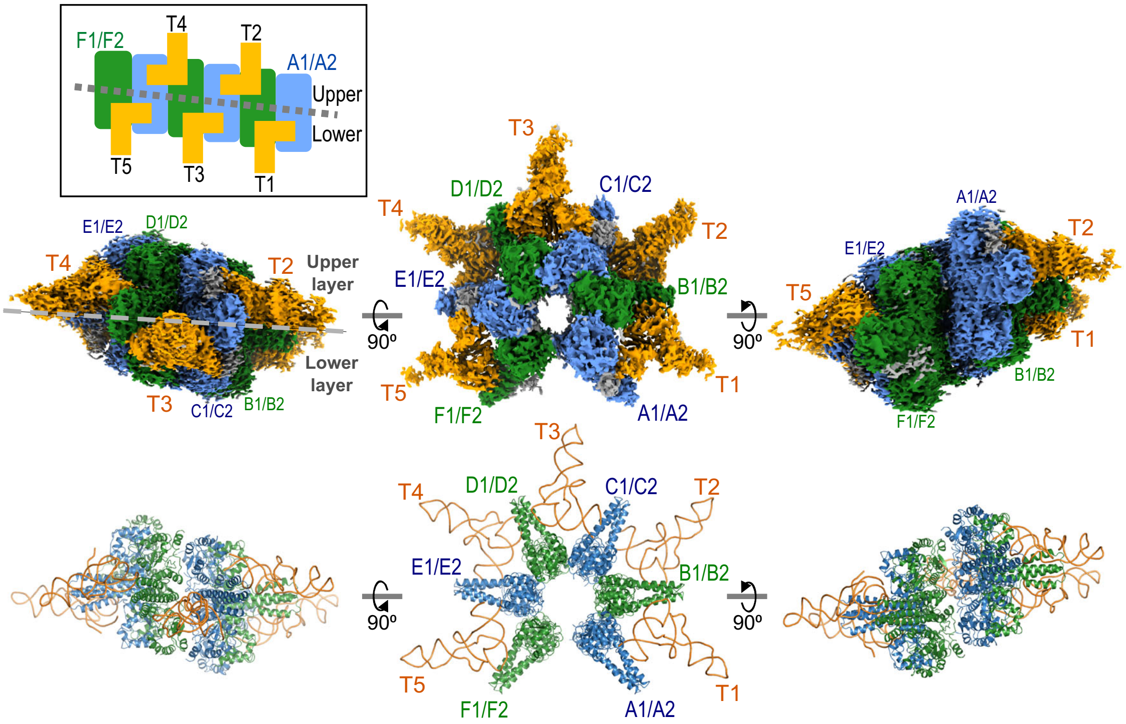

Fig. 1 | Cryo-EM structure of the *Aa*HARP:pre-tRNA complex. The cryo-EM map reconstruction (top) of the *Aa*HARP:pre-tRNA complex in different orientations is also shown in the cartoon mode at the bottom. The recognition and catalytic dimers are colored in green (B1/B2, D1/D2, and F1/F2) and blue (A1/A2, C1/C2, and E1/E2), respectively. A1, B1, C1, D1, E1, and F1 are the protomers of the lower layer. The bound pre-tRNAs are colored in orange (T1-T5). The gray potential map represents unmodeled regions due to weak maps. The simplified binding model is shown at the top left.

pre-tRNA recognition by HARPs

Our cryo-EM structures have revealed that the HARP dodecamer recognizes the elbow region and also the acceptor stem and the 5′-region around the cleavage site of pre-tRNA; furthermore, the structures elucidated that HARPs do not recognize specific substrate bases, but rather interact with the phosphate backbone (Fig. 2a–e). The overall volume of the pre-tRNA was visualized (Fig. 2a); however, the map corresponding to 5′-leader nucleotides was not clear enough to build a model. Consequentially, the pre-tRNA models only included nucleotides (nt) + 1 to + 72. The interaction modes of the five bound pre-tRNAs were identical. All four protomers in the adjacent catalytic and recognition dimers were involved in the recognition of one pre-tRNA (Fig. 2a, enlarged image on the right). As the pre-tRNA binding modes of *Aa*HARP and *Ht*HARP were identical (Fig. 2a–e and Supplementary Fig. 12), we focused on the C1/C2 and D1/D2 dimers of *Aa*HARP and T3 pre-tRNA, which showed the highest local resolution in our cryo-EM structure, to describe HARP:pre-tRNA interactions. The nuclease domain of the C1 protomer catalyzes the removal of the 5′-leader from pre-tRNA T3; residues in the PrH domains of C1, C2, D1, and D2 contribute to substrate binding.

*Aa*HARP recognizes the TψC arm that forms the “elbow” region of the L-shaped tRNA. Four arginine residues (Arg102, Arg109, Arg125, and Arg129) and one asparagine residue (Asn98) of the D1/D2 dimer contact the backbones of the TψC arm (Fig. 2b). The side chains of Arg102 and Arg109 in the D2 protomer form salt bridges with the phosphate moieties of nt + 54 and + 57, respectively. In addition, the side chain of Arg109 interacts with the ribose moiety of nt + 56. The side chains of Arg125 and Arg129 in the D1 protomer form both salt bridges with two phosphate moieties at positions + 56/ + 57 and + 54/ + 55, respectively. The side chain of Asn98 in the D2 protomer interacts with the phosphate moiety of nt +53. Three arginine residues (Arg102, Arg125, and Arg129) are highly conserved, whereas Asn98 and Arg109 are less conserved among HARP enzymes (Supplementary Fig. 13). This elbow-binding mechanism is similar to that previously observed in the crystal structure of the *Planctomycetes bacterium* HARP (*Pb*HARP) tetramer:pre-tRNA complex[50] (Supplementary Fig. 12).

In addition to the elbow recognition by the recognition dimers, the catalytic dimers contact the acceptor stem and can recognize the 5′-region around the cleavage site of pre-tRNA. Previous studies could not specify the regions interacting with the residues or their binding modes (Supplementary Fig. 9b–d). The cryo-EM structures obtained in the study presented here showed that three basic residues (Lys99, Arg123, and Lys127) in the C1 protomer are involved in acceptor stem recognition (Fig. 2c). Arg123 and Lys127 form salt bridges with the phosphate moieties of nt + 69 and + 68, respectively. Lys99 potentially contacts the phosphate moieties of nt + 67. Basic amino acids are well conserved at position 99. Lys127 is moderately conserved, while Arg123 is less conserved (Supplementary Fig. 13). As for recognizing the 5′-region around the cleavage site, Arg94 in the C2 protomer and Arg133 in the C1 protomer are spatially aligned and potentially contact the phosphate moieties of nt − 1 and + 1, respectively (Fig. 2d). These two arginine residues are highly conserved (Supplementary Fig. 13).

To evaluate the involvement of these residues in pre-tRNA recognition, we measured the binding affinity of the *Aa*HARP variants for a 5′-fluorescein-pre-tRNA substrate using fluorescence polarization (FP) analysis (Fig. 2f and Supplementary Fig. 14). The results of the mutational analysis suggest that the elbow-interacting residues (Arg102, Arg109, Arg125, and Arg129) and potential cleavage site-interacting residues (Arg94 and Arg133) are dominant contributors to pre-tRNA recognition. In contrast, the acceptor stem-interacting residues appear to recognize the pre-tRNA secondarily. This can be inferred from the FP assay showing that the R102A, R109A, R125A, and R129A variants of the elbow-interacting residues are severely defective in pre-tRNA binding. The R125A and R129A variants were previously demonstrated to exhibit severe kinetic defects[40]. The

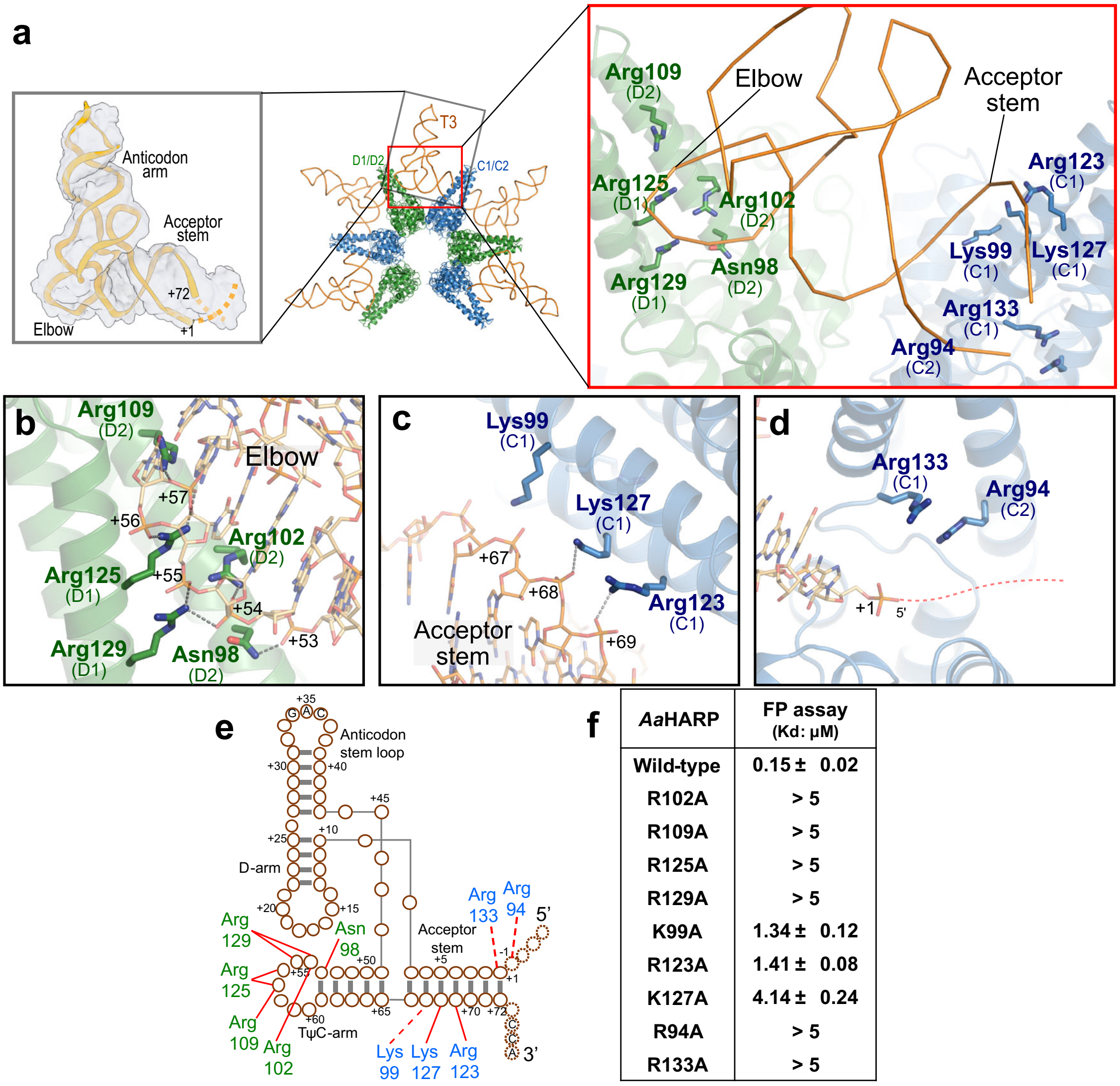

*Aa*HARP	FP assay (Kd: μM)
Wild-type	0.15 ± 0.02
R102A	> 5
R109A	> 5
R125A	> 5
R129A	> 5
K99A	1.34 ± 0.12
R123A	1.41 ± 0.08
K127A	4.14 ± 0.24
R94A	> 5
R133A	> 5

Fig. 2 | Interfaces between *Aa*HARP and pre-tRNA. a Potential map around the pre-tRNA, with the pre-tRNA cartoon model docked into the map (left). A close-up view of the *Aa*HARP:pre-tRNA interface is shown on the right, focusing on the C1/C2 and D1/D2 dimers. *Aa*HARP interacts predominantly with the phosphate backbones of the bound pre-tRNA. **b** Interface between *Aa*HARP and the elbow region. **c** Interface between *Aa*HARP and acceptor stem. **d** Interface between *Aa*HARP and the 5′-region around the cleavage site. **e** L-shaped 2D tRNA structure with tRNA-contacting residues of *Aa*HARP. Dashed-circle nucleotides represent unmodeled regions. **f** FP assay of *Aa*HARP wild-type and variants. Kd values were determined from three technical replicates. Errors indicate SEM. Source data are provided as a Source Data file.

R125A variant was almost inactive, and the R129A mutant showed complete inactivity. These results are in line with our FP assay findings. In addition, R94A and R133A variants of the proposed 5′-cleavage site-contacting residues also displayed a substantial loss of binding affinity. In contrast, Ala substitution of the basic residues that interact with the acceptor stem (K99A, R123A, and K127A) reduced the binding affinity by more than 10-fold, but substrate binding remained detectable in our assay. Therefore, we found that the elbow and the potential 5′-cleavage site-interacting residues play a crucial role in pre-tRNA recognition by HARPs.

Catalytic mechanism of HARPs

The cryo-EM structures provide insight into the catalytic mechanisms of HARPs. Other RNase P enzymes use two divalent metal ions to catalyze the hydrolysis of a phosphodiester bond between nt −1 and +1 in pre-tRNA, forming a mature 5′-end (+1 nt) containing a phosphate[22,27–30,41]. Our cryo-EM structures showed that the phosphate moiety at the +1 position is located in the active site of the catalytic dimers (Fig. 3a, b). The cryo-EM structures also showed that five acidic residues (Asp7, Asp138, Glu141, Asp142, and Asp160 in *Aa*HARP and Asp7, Asp140, Glu143, Asp144, and Asp162 in *Ht*HARP) and three hydrophilic residues (Thr8, Ser9, and Ser139 in *Aa*HARP and Thr8, Ser9, and Ser141 in *Ht*HARP) are clustered in the active sites of the catalytic dimers (Fig. 3a, b). These eight residues are derived from the same protomer and are highly conserved among HARP enzymes (Fig. 3a, b, and Supplementary Fig. 13). The structural arrangement of the five acidic residues and the scissile +1 phosphate moiety is conserved between HARPs and eukaryotic PRORPs, such as in the structure of *Arabidopsis thaliana* PRORP1[41] (*At*PRORP1) and *Homo sapiens* PRORP[47] (*Hs*PRORP) (Fig. 3c, d).

To assess the catalytic functionality of the eight residues constituting the HARP active sites, we analyzed the cleavage activities of the D7N, T8A, S9A, D138N, S139A, E141Q, D142N, and D160N variants of *Aa*HARP (Fig. 3e). Variants D7N, S139A, E141Q, D142N, and D160N were inactive and the D138N mutation had a moderate effect on cleavage activity. In contrast, the T8A and S9A variants exhibited activities

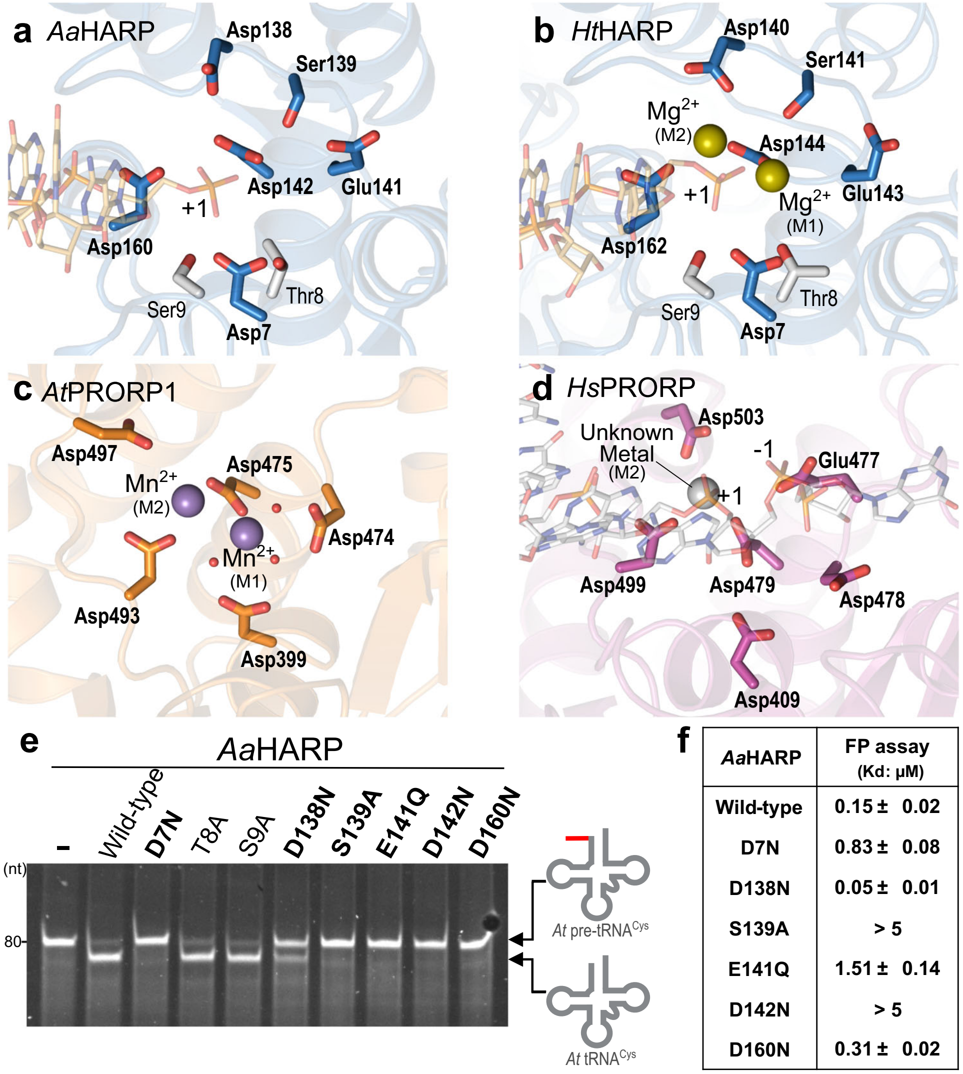

*Aa*HARP	FP assay (Kd: μM)
Wild-type	0.15 ± 0.02
D7N	0.83 ± 0.08
D138N	0.05 ± 0.01
S139A	> 5
E141Q	1.51 ± 0.14
D142N	> 5
D160N	0.31 ± 0.02

Fig. 3 | Active sites of protein-based RNase P. Comparison of active sites among protein-based RNase P: (**a**) *Aa*HARP, (**b**) *Ht*HARP, (**c**) *At*PRORP1, and **d** *Hs*PRORP. Residues and the bound metals in the active sites are shown as stick and sphere models, respectively. The bound pre-tRNAs are shown in the stick mode with 50% transparency. **e** A representative TBE-urea gel of pre-tRNA^{Cys} in vitro processing by the *Aa*HARP wild-type enzyme and variants thereof. The processing assay was performed in three independent replicates. **f** FP binding assay results for the *Aa*HARP wild-type protein and variants thereof. Kd values were determined from three technical replicates. Errors indicate SEM. Source data are provided as a Source Data file.

comparable to those of the wild-type enzyme. Therefore, we conclude that five acidic residues (Asp7, Asp138, Glu141, Asp142, and Asp160) and one serine residue (Ser139) play key roles in catalysis and/or active site architecture. The dissociation constants (Kd) of these six key residue variants were determined by the FP assay (Fig. 3f and Supplementary Fig. 14). The S139A and D142N variants abolished pre-tRNA binding. E141Q reduced the binding affinity by 10-fold, while variants D7N, D138N, and D160N showed binding affinities comparable to that of the wild-type enzyme, indicating that their function is directly in catalysis.

These results are in line with previous studies on eukaryotic PRORPs, in which key acidic residues have been proposed to form either direct or water-mediated contacts with two divalent metal ions (M1 and M2)[41,43,45,51]. Our mutational analyses confirmed the catalytic importance of the four aspartates, one glutamate, and one serine residue in *Aa*HARP (Fig. 3e), suggesting that these residues are involved in the coordination of M1 and M2. In a previous study, Asp475 of *At*PRORP1, which is structurally equivalent to Asp142 of *Aa*HARP, was proposed to play a crucial role in metal ion coordination via direct interactions[41]. Therefore, the D142N variant of AaHARP may lose its metal-binding capacity and/or fail to form active sites. We speculate that this is the reason behind its impaired catalytic and substrate-binding abilities (Fig. 3e, f). A similar phenotype was observed for the S139A variant of *Aa*HARP. Ser139 of *Aa*HARP is structurally equivalent to Ser141 of *Ht*HARP, and eukaryotic PRORPs do not have any corresponding residues. As Ser141 of *Ht*HARP is located near the M1 metal position, the Ala substitution is likely to have a severe effect on metal ion coordination and/or the formation of the active sites. In contrast, Asn/Gln substitution of the other acidic residues (Asp7, Asp138, Glu141, and Asp160) maintains compatibility with substrate binding (Fig. 3f), which suggests these mutations do not destroy the active site architecture, but may disrupt the coordination of one or both catalytic metal ions to explain the catalytic inactivity of these mutant enzymes. The carboxylic acid (-COO$^-$) moieties of the acidic residues are suggested to play an essential role in the catalytic process.

Potential maps indicating the presence of two Mg^{2+} ions were observed at an active site in the cryo-EM reconstitution of the *Ht*HARP:pre-tRNA complex (Fig. 3b). Despite the addition of excess magnesium to the protein solution, maps for two metal ions were observed in only one out of twelve active sites, indicating a potentially low binding affinity for Mg^{2+} ions. However, previous studies demonstrated that Mg^{2+} is essential for HARP activity[36,39,40], and this study shows structural arrangements and roles of the proposed metal-coordinating residues are similar to those of previous studies on *At*PRORP1 and *Hs*PRORP (Fig. 3 and Supplementary Fig. 15). Therefore, we assumed that the observed potential maps in the active sites corresponded to two Mg^{2+} ions. The *Ht*HARP:pre-tRNA complex revealed that two metals in the active site coordinate the oxygen of the scissile phosphodiester between nt −1 and +1 (Fig. 3b). This coordination is consistent with the two-metal catalytic mechanism proposed for the *At*PRORP1 structure[41]. The proposed theoretical metal coordination model (Supplementary Fig. 15) is also in agreement with the metal position and conformation of the residues in the active site of the *Ht*HARP:pre-tRNA complex, albeit requiring slight conformational changes. We propose that HARPs employ a two-metal ion catalytic mechanism, similar to that of other RNase P enzymes. Overall, we propose that Asp142/Asp144 of *Aa*/*Ht*HARP form inner-sphere direct interactions with one or both metal ions; the other key residues may be involved in inner- or outer-sphere metal ion coordination as well or in other aspects of the catalytic process (e.g., acting as general acid or base). Notably, a previous study proposed that Asp399 of *At*PRORP1 activates one metal-bound water molecule for the nucleophilic attack at the phosphorus atom of nt +1[41]. The Asp7 residues of *Aa*HARP and *Ht*HARP are structurally equivalent to Asp399 in *At*PRORP1 (Fig. 3 and Supplementary Fig. 15), proposing that Asp7 could function as a catalytic base.

*Aa*HARP processes the pre-tRNA 3′-trailer

The structures obtained provided insights into the HARP 5′-leader processing mechanism and revealed that the productive HARP dodecamer binds five pre-tRNA molecules rather than ten pre-tRNAs predicted previously[39]. The finding indicates that seven of the 12 active HARP dodecamer sites remained vacant. As detailed below, our cleavage assays also revealed 3′-trailer processing capability, which may assign a biological function to these vacant sites. When we utilized *A. thaliana* pre-tRNA^{Cys} carrying a 50-nt 5′-leader and a 30-nt 3′-trailer (Supplementary Fig. 6), we detected two tRNA products and a 50-nt 5′-leader processed by *Aa*HARP (Supplementary Fig. 16). One tRNA product corresponded to 5′-mature tRNA^{Cys} with the 30-nt 3′-trailer, and the other to 5′-mature tRNA^{Cys} with a partially shortened 3′-trailer. The cleavage assay also showed that the longer tRNA product decreased with increasing *Aa*HARP concentration (Supplementary Fig. 16).

Using mass spectrometry (MS), we identified the second cleavage product to result from 3′-trailer processing of *Aa*HARP (Fig. 4a). MS analysis identified the cleavage site on the substrate *A. aeolicus* pre-tRNA^{Val}, which contains a 4-nt 5′-leader and 30 nt 3′-trailer sequences. After the enzymatic reaction with *Aa*HARP, we analyzed the small fragment products and observed two cleavage products (Fig. 4a and Supplementary Data 1 and 2). First, we observed a prominent peak with an *m/z* value of 1327.24. The observed *m/z* value of this RNA product corresponds well with the theoretical *m/z* value (1327.21) of 5′-pGCAA$_{OH}$-3′, the 5′-leader sequence expected for processing at the canonical site. The other prominent peak was detected at *m/z* 5765.10, corresponding to 5′-pGCGCUUAAUAAAAA UUCC$_{OH}$-3′ (theoretical *m/z* value: 5765.484), the last 18 nucleotides of the 30-nt 3′-trailer. The results revealed that *Aa*HARP cleaves the phosphodiester bond between nt +85 and +86 in the 3′-trailer region, 13 nucleotides downstream of the last base-paired nt +72 in the acceptor stem (Fig. 4a).

We conducted additional experiments to investigate *Aa*HARP 3′-processing and uncovered four distinct characteristics: the cleavage position varied depending on the pre-tRNA sequence, the 5′-leader nucleotides appeared to be unnecessary, the tRNA structure was necessary, and the *Aa*HARP dodecamer active sites were utilized. To assess the 3′-cleavage position of another *A. aeolicus* pre-tRNA sequence, we compared the cleavage products obtained with *A. aeolicus* pre-tRNAs (pre-tRNA^{Val}, tandem pre-tRNA$^{Gly\text{-}Thr}$, pre-tRNA^{Gly}, and pre-tRNA^{Thr}) (Fig. 4b). The pre-tRNA$^{Gly\text{-}Thr}$ tandem transcript derived from the *A. aeolicus tufA2* operon was used as a model substrate for tRNA processing enzymes in previous studies[52,53]. The separated pre-tRNA^{Gly} and pre-tRNA^{Thr} carried 32 nt and 30 nt 3′-trailer, respectively (Supplementary Fig. 6). *Aa*HARP exhibited distinct processing patterns depending on the pre-tRNA sequence. In the pre-tRNA^{Thr} processing [Thr(0,30) in Fig. 4b], we observed a similar product to the 13-nt 3′-trailer that was the single major product obtained with *A. aeolicus* pre-tRNA^{Val} [green asterisk of the Thr(0,30) lane]. Using MS, we identified this product as pre-tRNA^{Thr} carrying the 16 nt 3′-trailer (Supplementary Fig. 17 and Supplementary Data 3 and 4). In addition, we observed a slightly longer 3′-processing intermediate than the product with 16 nt 3′-trailer [light blue asterisk of the Thr(0,30) lane]. In the pre-tRNA^{Gly} processing [Gly(0,32) in Fig. 4b], no predominant product by 3′-trailer processing was detected; instead, only minor quantities of longer 3′-processing intermediates were observed [light blue asterisk of the Gly(0,32) lane]. As for the tandem pre-tRNA processing (Tandem in Fig. 4b), we can interpret products from the processing patterns of isolated pre-tRNA^{Gly} and pre-tRNA^{Thr}. We observed three 5′-processing products cleaved at the canonical site [red asterisks of the Tandem lane: Tandem without 5′-leader as well as 5′-mature Gly(0,32) and Thr(0,30)]. In addition, a product with the 3′-trailer shortened to 16 nt (green asterisk at the Tandem lane) and 3′-processing intermediates (light blue asterisks at the Tandem lane) were observed. The product with the 16 nt 3′-trailer (green asterisk of the Tandem lane) and 3′-processing intermediates (light blue asterisks of the Tandem lane). These imply that the *Aa*HARP 3′-cleavage position depends on the pre-tRNA sequence and that the 3′-trailer region is cleaved at a minimum of 13 nucleotides downstream of the last base-paired nucleotide in the acceptor arm. Moreover, the results of pre-tRNA^{Val} and pre-tRNA^{Thr} processing suggest that HARP may cut RNA nucleotides after adenine base (Fig. 4a and Supplementary Fig. 17). Next, to evaluate the effect of the presence or absence of the 5′-leader nucleotides on 3′-processing, we used *A. aeolicus* pre-tRNA^{Val} lacking 5′-leader and carrying the 30 nt long 3′-trailer [Val(0,30), Supplementary Fig. 6]. *Aa*HARP also exhibited the 3′-trailer processing activity in the absence of the 5′-leader [the Val(4,30) lanes versus Val(0,30) lanes in Fig. 4b]. Moreover, to investigate the tRNA specificity of 3′-processing by *Aa*HARP, we used a 31 nt long single-stranded RNA with a sequence identical to the 3′-trailer of pre-tRNA^{Val}. *Aa*HARP displayed no cleavage activity on the 31 nt long single-strand RNA (the 31 mer lanes in Fig. 4b), indicating the indispensability of the tRNA structure for the 3′-trailer processing capability of *Aa*HARP. Finally, we verified that *Aa*HARP utilizes its own active sites to catalyze the 3′-trailer processing of pre-tRNA. For this purpose, we used variants (D7N, D138N, E141Q, and D160N) that were defective in 5′-leader processing but retained pre-tRNA binding affinity (Fig. 4c), and tested the 3′-trailer processing ability of these variants for *A. aeolicus* pre-tRNA^{Val} carrying the 30-nt 3′-trailer. These catalytic mutant proteins were inactive in 3′-trailer processing, demonstrating that *Aa*HARP active sites were responsible for 3′-trailer and 5′-leader processing. Thus, we could exclude the possibility that *Aa*HARP preparations were contaminated with other 3′-trailer processing activities. Finally, we demonstrated that *Ht*HARP also catalyzes 5′-leader and 3′-trailer processing in a pattern similar to that of *Aa*HARP (Fig. 4c).

In summary, we identified a unique HARP 3′-trailer processing mechanism that has not been observed for any other type of RNase P enzyme. Cleavage assays suggested that HARPs primarily remove the 5′-leader sequence and process 3′-trailer nucleotides secondarily, employing the vacant active sites in the HARP:pre-tRNA complex to catalyze this unique 3′-trailer processing reaction.

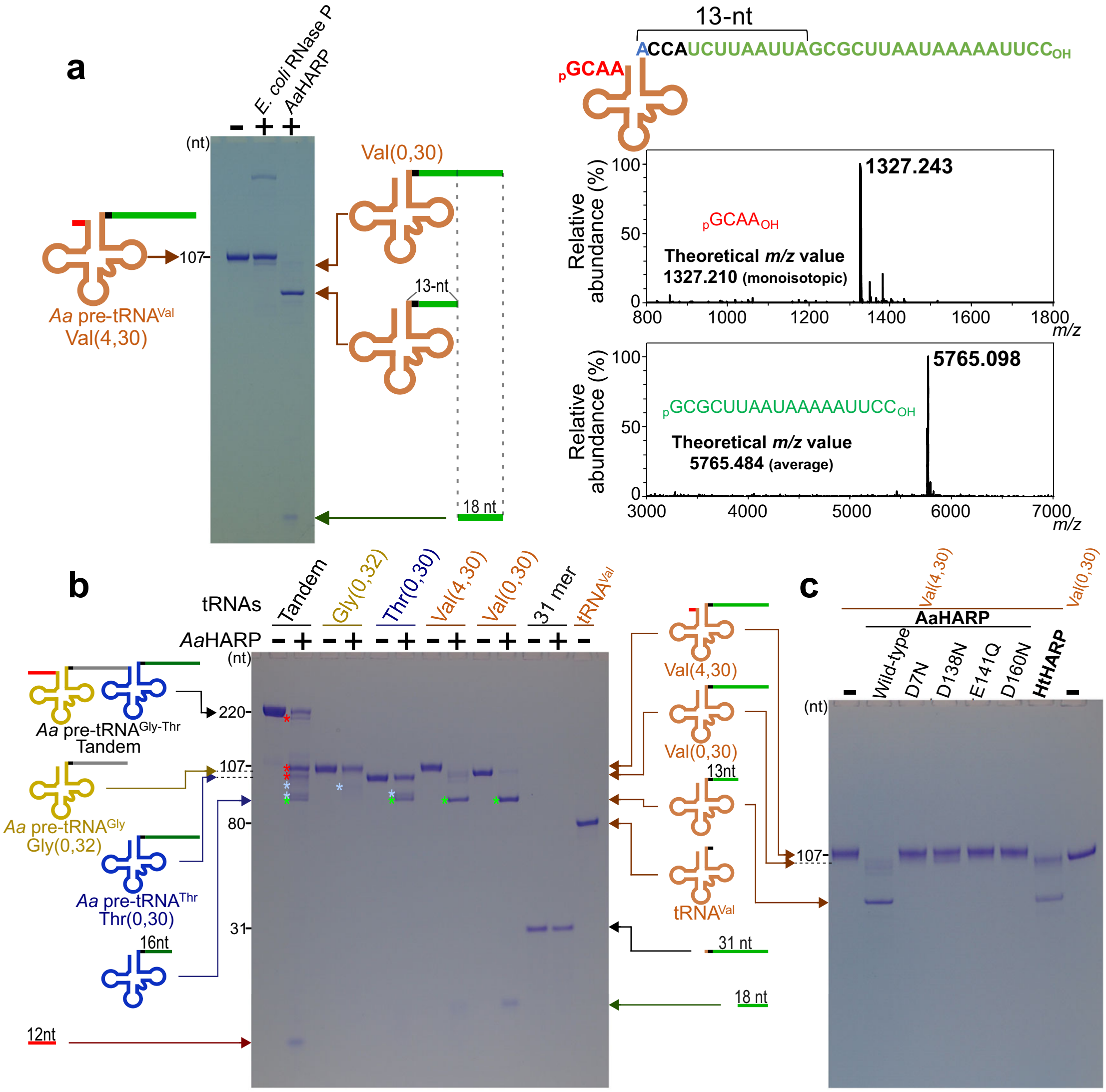

Fig. 4 | *Aa*HARP 3′-trailer processing assay. a (right) *Aa*HARP and *Escherichia coli* RNA-based RNase P processing pattern for *A. aeolicus* pre-tRNA^{Val} carrying 4-nt 5′-leader / 30-nt 3′-trailer. (left) MS spectra confirm the identity of *Aa*HARP 5′-processing product 5′-$_{p}$GCAA$_{OH}$-3′ and 3′-processing product 5′- $_{p}$GCGCUUAAU AAAAAUUCC$_{OH}$-3′. **b** *Aa*HARP 3′-trailer processing pattern for different pre-tRNAs. Red, green, and light blue asterisks represent (red) 5′-processing products cleaved at the canonical site, (green) the proposed 3′-processing product carrying 13–16 nt long 3′-trailers, and (light blue) a 3′-processing intermediate that is longer than the product with the 16 nt 3′-trailer, respectively. **c** 3′-trailer processing of pre-tRNA [Val(0,30)] by wild-type *Aa*HARP, wild-type *Ht*HARP, and active site mutants of *Aa*HARP. TBE-urea gel images of the cleavage assays are representative of three independent replicates. Source data are provided as a Source Data file.

Discussion

The cryo-EM structures obtained in this study provide an overall picture of pre-tRNA 5′-leader processing by HARPs. The structure-guided mutational analysis demonstrated that the elbow region and 5′-cleavage site are hotspots for HARP substrate recognition. Key residues for pre-tRNA recognition are highly conserved among HARPs. Our study confirms that HARPs function as molecular rulers that sense the invariant distance between the elbow region and pre-tRNA 5′-cleavage site (Fig. 5).

The HARP:pre-tRNA structure determination enabled comprehensive comparisons of (pre-)tRNA binding modes and active site architectures across different types of RNase P:substrate complexes[22,47] (Fig. 5), suggesting that RNase P enzymes interact with the tRNA elbow and the 5′-cleavage site in a conceptually similar manner, thereby achieving the function of a molecular ruler[54]. There were slight variations in the elbow recognition mode among RNase P enzymes. HARPs specifically recognize the TψC-loop of the pre-tRNA elbow region via involvement of several basic residues. Eukaryotic PRORPs utilize aromatic residues for stacking interactions with tRNA elbow bases, in addition to electrostatic interactions between basic residues and the elbow region. RNA-based RNase P enzymes predominantly recognize the elbow region via base-base stacking interactions[21–24]. This study suggests that the basic residues of HARPs may potentially interact with the phosphate backbones of the 5′-leader nucleotides. Previous studies have shown that basic residues of PRORPs and RNA-based RNase P protein components also interact with the phosphate backbones of the 5′-leaders[22,23,47]. These imply that the utilization of basic residues for contacting 5′-leader nucleotides seems to be a common feature among RNase P enzymes. Furthermore, all RNase P enzymes are likely to employ a two-metal ion mechanism[22,27,30,41].

As different types of RNase P enzymes catalyze identical reactions, RNase P enzymes are excellent targets for understanding enzyme diversity and its molecular evolution. HARPs function as molecular rulers via oligomerization, effectively positioning the PrH domain relative to the nuclease domain. In comparison, eukaryotic PRORPs

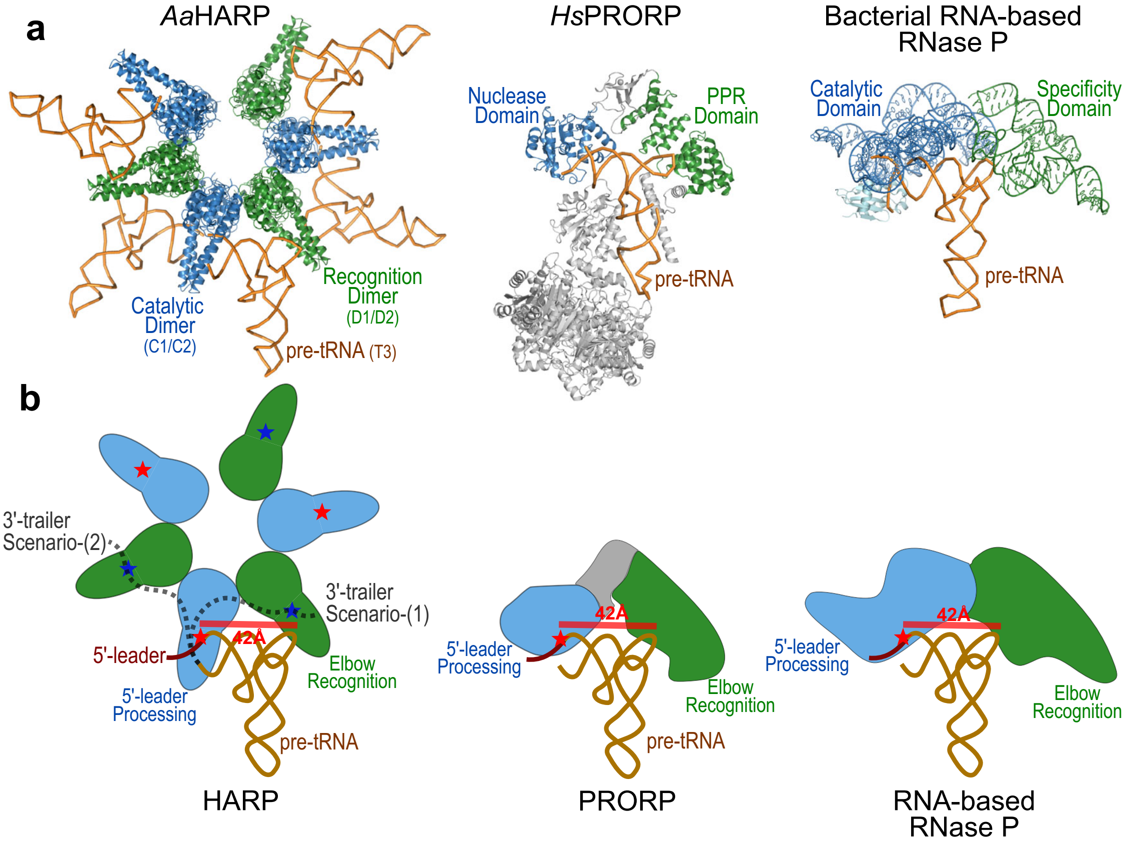

Fig. 5 | Architectural diversity of RNase P enzymes and their common concept of substrate recognition. **a** Structures of *Aa*HARP (left), *Hs*PRORP (middle, PDB id 7ONU), and RNA-based RNase P (right, PDB id 3Q1R) in the cartoon mode. The elbow-contacting and active-site-containing portions are colored in green and blue, respectively. The bound (pre-)tRNAs are colored in orange. *Hs*PRORP requires two additional protein cofactors for activity (gray). **b** Simplified models for all types of RNase P enzymes, illustrating their shared function as molecular rulers. The catalytic centers for 5′-leader processing are marked by red stars, pre-tRNAs are gold-colored, and 5′-leader regions of pre-tRNAs are colored in deep red. As for the HARP model, a representative single pre-tRNA is displayed. 3′-trailer regions are shown as gray-dash lines. Additional catalytic centers potentially utilized for 3′-trailer processing are shown as blue stars. There are two potential scenarios for 3′-trailer processing.

function as molecular rulers via a PPR domain fused to a nuclease domain at the appropriate position. The RNA component of RNA-based RNase P consists of two domains: the catalytic domain (C-domain) responsible for the cleavage reaction and the specificity domain (S-domain) dedicated to binding the tRNA elbow[19,21]. The pre-configured interdomain orientation allows for the measurement of the distance between the elbow and the cleavage site (Fig. 5). Despite the divergent forms exhibited by all types of RNase P, these enzymes converged towards a shared concept of tRNA recognition (Fig. 5).

The presented structures revealed that the HARP dodecamer can bind five pre-tRNAs; thus, seven of the 12 active sites in the HARP dodecamer remain vacant, indicating that the catalytic capacity of HARPs is underutilized in the 5′-leader processing reaction. This underutilization is partially offset by the 3′-trailer activity discovered here. Cleavage assays revealed that the *Aa*HARP 3′-cleavage position is at a minimum of 13 nt downstream of the last base-paired nucleotide in the acceptor stem. Mutational analysis suggested that the active sites of HARP dodecamers catalyze 5′-leader and 3′-trailer processing (Fig. 4c). In the cryo-EM structures, the active sites of catalytic dimers were occupied by scissile phosphodiesters of the tRNAs poised for 5′-end maturation, while active sites of neighboring recognition dimers remained vacant (Supplementary Fig. 18); hence, we hypothesize that the *Aa*HARP dodecamer cleaves the 3′-trailer nucleotides at the vacant active sites of the neighboring recognition dimers. The structures indicated that neighboring vacant active sites on the same layer of the two-layer HARP dodecamer are approximately 41–44 Å away from the last base-paired 3′-nt +72 of the bound pre-tRNA in the catalytic dimer (Supplementary Fig. 18), while neighboring vacant active sites in the different layer were approximately 53–55 Å away from the position of nt +72 (Supplementary Fig. 18). The 3′-trailer seems to reach neighboring vacant active sites on the same layer without steric hindrance. In contrast, the 3′-trailer appears to require a long-detoured conformation to reach neighboring active sites on different layers due to potential steric hindrance with the PrH domain and bound pre-tRNA. Therefore, 3′-trailer processing is likely to occur in neighboring vacant active sites on the same layer (Supplementary Figs. 18 and 19a). The 41–44 Å distance in the same layer corresponds to eight nucleotides in an RNA chain because the distance between two phosphorus atoms of two consecutive nucleotides is approximately 5.5 Å. Therefore, 13 nucleotides may be the shortest distance for reaching neighboring vacant active sites without steric hindrance. The docking simulation results support this hypothesis (Supplementary Fig. 19b). Two vacant active sites on the same layer are present in proximity to the 5′-leader processing site, thus providing two potential scenarios for 3′-trailer processing. In both scenarios' model, a 3′-trailer longer than 13 nt can reach the vacant active center without steric hindrance (Fig. 5 and Supplementary Fig. 19b).

The acquisition of accessory 3′-trailer processing in addition to the primary 5′-leader processing by HARP might be a reasonable solution for facilitating pre-tRNA maturation. Generally, unlike 5′-leader processing which is mediated exclusively by RNase P in all types of cells, 3′-trailer processing is carried out by a diverse repertoire of endoand exo-ribonucleases[55–57]. Bacteria possess two pathways for 3′-processing[55,56]. Hence, 3′-trailer processing in *A. aeolicus* is also thought to involve two pathways (Supplementary Fig. 20). For pre-tRNAs without the encoded CCA sequence, RNase Z (Uniprot ID: A0A9D0YQJ8_AQUAO, gene name: unclear) finally removes 3′-trailer nucleotides, and the 3′-terminal CCA residues are added by CC- and A-adding enzyme (Uniprot ID: CATNT_AQUAE/AATNT_AQUAE, gene name: *aq_2158*/*aq_411*)[58,59]. It remains unclear whether *A. aeolicus* possesses RNase Z or not. The other pathway involves pre-tRNAs containing genome-encoded CCA sequences (Supplementary Fig. 20), wherein the endoribonuclease RNase G (*Aa*Rng) (Uniprot ID: O67311_AQUAE, gene name: *aq_1275*) initially produces processing intermediates with extra 3′ nucleotides[52,60]. Subsequently, exoribonucleases such as RNases PH trim the 3′-trailer to generate the 3′-mature CCA end[53,61]. Of the 44 tRNA genes, 36 encode the CCA nucleotide[62]; hence, this mechanism appears to be the dominant pathway in *A. aeolicus*. To our knowledge, the precise length of the 3′-trailer in *A. aeolicus* pre-tRNAs has not been thoroughly investigated. Recent genome-wide RNA sequencing analyses in other bacteria have revealed that several 3′-untranslated regions are considerably longer than the previously estimated 40–50 nucleotides[63,64]. *E. coli* is likely not representative for *A. aeolicus*, considering that *E. coli* has a genome of 4.6 Mbp, whereas the *A. aeolicus* genome is highly condensed, with a length of only 1.6 Mbp. Nevertheless, in bacterial systems, cleavage by endonucleases generally initiates the 3′-processing step for pre-tRNA in bacteria[56,65,66]. This study suggests that *Aa*HARP emerges as a candidate enzyme involved in the initial 3′-processing step. Therefore, we conducted a comparative analysis of the 3′-processing activities between *Aa*HARP and *Aa*Rng. *Aa*Rng processed 3′-trailer on *A. aeolicus* pre-tRNA$^{\mathrm{Val}}$, a pattern different from that observed in *Aa*HARP processing (Supplementary Fig. 21a), and the time course for the reaction showed both enzymes have similar 3′-trailer processing capabilities (Supplementary Fig. 21b), suggesting that the 3′-processing activity *Aa*HARP is redundant with that of *Aa*Rng. The redundancy of 3′-processing enzymes is known in bacteria; in *E. coli*, RNase E[65–67], RNase G[67], RNase III[68], and RNase BN[67,69,70] were reported to catalyze endonucleolytic cleavage of pre-tRNA 3′-trailers. Therefore, we propose that *Aa*HARP is another endoribonuclease in the dominant pathway. Moreover, we cannot rule out the possibility that the 3′-processing by *Aa*HARP occurs before the 3′-trailer removal by RNase Z in the pathway for pre-tRNA without CCA (Supplementary Fig. 20). Further studies are needed to fully explore the 3′-processing pathway in the Aquificaceae. However, this study proposes a framework for elucidating tRNA maturation mechanisms in the Aquificaceae.

The genome of *A. aeolicus* encodes seven polycistronic tRNA operons (tRNA$^{\mathrm{Gly}}$-tRNA$^{\mathrm{Cys}}$, tRNA$^{\mathrm{Ile}}$-tRNA$^{\mathrm{Ala}}$, tRNA$^{\mathrm{Ile}}$-tRNA$^{\mathrm{Ala}}$, tRNA$^{\mathrm{Arg}}$-tRNA$^{\mathrm{Lys}}$, tRNA$^{\mathrm{Thr}}$-tRNA$^{\mathrm{Tyr}}$-tRNA$^{\mathrm{Gly}}$-tRNA$^{\mathrm{Thr}}$, tRNA$^{\mathrm{Glu}}$-tRNA$^{\mathrm{Val}}$, and tRN$^{\mathrm{Ala}}$-tRNA$^{\mathrm{Lys}}$) (Supplementary Fig. 22a). Our cleavage assay using in a tandem pre-tRNA indicated that both 5′-processing and 3′-processing take place (Fig. 4b). We cannot rule out the possibility that the binding mode of HARP to the five pre-tRNAs works as a pre-set mechanism for processing these tandem pre-tRNAs. The lengths of intercistronic regions of dimeric precursors range from 11 to 28 nt (Supplementary Fig. 22a). The docking simulation shows that a linker of 11 nt connecting two adjacent tRNAs (e.g., T2 and T3 in Fig. 1) allows their binding to the active sites of the same catalytic dimer without steric hindrance (Supplementary Fig. 22b left). In the tetracistronic tRNA$^{\mathrm{Thr}}$-tRNA$^{\mathrm{Tyr}}$-tRNA$^{\mathrm{Gly}}$-tRNA$^{\mathrm{Thr}}$ precursor, the intercistronic spacer sequences are 22, 12, and 32 nt in length. Thus, the tetracistronic precursor could also bind without steric hindrance to the four active sites of two neighboring catalytic dimers within the HARP dodecamer (Supplementary Fig. 22b right). In this binding mode, intercistronic regions can approach the vacant 3′-processing site of the recognition dimers, suggesting a potential mechanism for processing at intercistronic regions of the multimeric precursor. Further biochemical and structural studies will be necessary to understand the intricacies of this process.

The Aquificaceae family, including *A. aeolicus* and *H. thermophilus*, seems to utilize oligomerization of the small protein HARP to achieve bifunctionality in pre-tRNA processing. Our findings illustrate an evolutionary strategy by which organisms with compact genomes can acquire multifunctionality through evolution.

Methods

Expression and purification of HARPs

We substituted a cysteine residue (Cys114) in *Aa*HARP with a serine residue to avoid undesired disulfide bond formation that could lead to aggregation (Supplementary Fig. 5). The protein expression and purification have previously been reported[39]. In brief, the cDNA sequences encoding *Aa*HARP (residues 1–192) and Hth1307 (residues 1–194) were subcloned into the pE_SUMO vector, which encodes an N-terminal His$_6$-SUMO tag. The cDNA sequences and primers are listed in Supplementary Table 2 and 3, respectively. Recombinant *Aa*HARP and *Ht*HARP were expressed in the *E. coli* strain BL21-CodonPlus (DE3)-RIL (Agilent Technologies). The proteins were first purified by Ni-NTA agarose chromatography (Fujifilm Wako Chemicals), and the eluted proteins were subsequently digested by Ulp1 to remove the SUMO-tag, followed by purification on a HiTrap Q (5 mL) column (Cytiva). The peak fractions containing the target proteins were pooled and concentrated. The proteins were further purified using a HiLoad 16/60 Superdex 200 column (Cytiva). The peak fractions were pooled and concentrated to 30 mg/mL.

Preparation of *Aa*HARP variants

*Aa*HARP variants were generated by site-directed mutagenesis using the NEBuilder assembly tool (New England Biolabs). The primers are listed in Supplementary Table 3. The variant proteins were purified using the same procedure as for the wild-type protein. Purified proteins were analyzed by size exclusion chromatography (Superdex 200 Increase 10/300 GL column) to assess their ability to assemble into the dodecamer, and no differences were observed between wild-type and variant proteins (Supplementary Fig. 23). The size exclusion chromatography column was equilibrated with 50 mM Tris-HCl, pH 8.0, 200 mM NaCl, 0.5 mM Tris(2-carboxyethyl)phosphine Hydrochloride (TCEP). The concentration of the loaded proteins was 5 mg/mL.

Construction of plasmid DNAs to synthesize a series of templates for in vitro transcription

We constructed three plasmid DNAs (pUC_AaValG1, pUC_Aa4Val30, and pUC_Aa12Gly-Thr30) to be used as PCR templates to synthesize a series of templates for in vitro transcription using T7 RNA polymerase.

For pUC_AaValG1, oligo-DNAs (Eurofins Genomics), Aae_ValG1_F; 5′-TAATACGACT CACTATAGGG CGCGTAGCTC AGTAGGGAGA GCG CCGGCCC GACACGCCGG AGGTCGGGGG-3′ (70 mer) and Aae_Val_R; 5′-TGATTACGCC AAGCTTGGTA GGCGCGGGGG GACTTGAACC CCCG ACCTCC GGCGTGTCGG GCCGGCGCTC-3′ (70 mer), were mixed and annealed. A double-stranded DNA was then synthesized with KOD DNA polymerase, and the resulting DNA was ligated with a plasmid DNA fragment amplified from pUC19 using the primers, pUC_Hind_F; 5′-AAGCTTGGCG TAATCATGGT C-3′ (21 mer) and pUC_T7_Pst_R; 5′-ATAGTGAGTC GTATTACTGC AGGTCGACTC TAGAGGAT-3′ (38 mer), by the patch cloning method[71] using T7 exonuclease, T7 DNA polymerase lacking 3′–5′ exonuclease activity, and T7 DNA ligase[72]. The nucleotide sequence of the resulting plasmid was confirmed.

For pUC_Aa4Val30, which encoded pre-tRNA$^{\mathrm{Val}}$ carrying a 4-nt 5′-leader and a 30-nt 3′-trailer, the pre-tRNA gene was amplified from pUC_AaValG1 with primers, T7_Aae_preVal_P; 5′-GGGGCTGCAG TAATACGACT CACTATAGCA AAGGCGCGTA GCTCAGTAGG GA-3′ (52 mer) and Aae_Val_30nt_R; 5′-TGATTACGCC AAGCTTGGAA

TTTTTATTAA GCGCTAATTA AGATGGTAGG CGCGGGGGGA CTTGAA-3′ (66 mer). The amplified DNA was inserted between the *Pst* I and *Hin*d III sites of pUC19. The nucleotide sequence of the resulting plasmid was confirmed.

For pUC_Aa12Gly-Thr30, oligo-DNAs, Aae_Gly_F; 5′-TATTACTGAG CGGGCGTAGC TCAGTTGGTA GAGCAGCGGC CTTCCAAGCC GCAGGTCGCG GGTTCGAGT-3′ (69 mer) and Aae_Gly_R; 5′-TTATTTATTG AAGGAAGGGA TTTTTATATT GGAGCGGGCG ACGGGACTCG AACCCGCGAC CTGCGGCTTG-3′ (70 mer), were mixed and annealed. At the same time, Aae_Thr_F; 5′-TCCCTTCCTT CAATAAATAA GCCCAGGTAG CTCAGTCGGT AGAGCGCACC CTTGGTAAGG GTGAGGGCGC-3′ (70 mer) and Aae_Thr_R; 5′-TAAAGAGGGA TTTTTATCAG GGAAGTGGAG CCCAGGACCG GACTCGAACC GGCGCCCTCA CCCTTACCAA-3′ (70 mer), were mixed and annealed. Each double-stranded DNA synthesized with KOD DNA polymerase was then purified by agarose gel electrophoresis. Both DNAs were mixed and used as PCR templates, as each DNA contains complementary regions. The PCR was performed with the primers, T7_Aae_preGly_P; 5′-TAATACGACT CACTATAGGA TATTACTGAG CGGGCGTAGC TCAGTTGGT-3′ (39 mer) and Aae_Thr_30nt_R; 5′-TGATTACGCC AAGCTTTGTA AAGAGGGATT TTTATCAGGG AAGTGGAGC-3′ (49 mer). The amplified DNA was purified by agarose gel electrophoresis. The purified DNA was ligated with a plasmid DNA fragment amplified from pUC19 with the primers, pUC_Hind_F and pUC_T7_Pst_R, by the patch cloning method[71] using T7 enzymes[72]. The nucleotide sequence of the resulting plasmid was confirmed.

Preparation of the phosphorothioate-modified pre-tRNA$^{\mathrm{Val}}$

To form a stable complex between *Aa*HARP and pre-tRNA, we prepared *A. aeolicus* pre-tRNA$^{\mathrm{Val}}$ substrate containing phosphorothioate modifications at four nucleotides (− 2, − 1, + 1, + 2 positions) in the vicinity of the cleavage position (Supplementary Fig. 6). Phosphorothioate modification renders the internucleotide linkage more resistant to nuclease degradation, typically as a racemic mixture (*S*p- and *R*p-forms) in which either of the two non-bridging phosphate oxygens is replaced by sulfur. A previous study demonstrated that *S*p-phosphorothioate modification exhibits more resistance to PRORP enzyme than *R*p-phosphorothioate modification[51]. Therefore, given our inability to separate the *S*p- and *R*p-forms, we confirmed that half of our prepared pre-tRNA derivatives exhibited resistance to *Aa*HARP activity.

To prepare the phosphorothioate-modified pre-tRNA$^{\mathrm{Val}}$, we ligated the first half (nt − 4 to + 34) and the 5′-phosphorylated last half (nt + 35 to + 76) of *A. aeolicus* pre-tRNA$^{\mathrm{Val}}$ as described above. The first half, containing phosphorothioate modifications at − 2, − 1, + 1, and + 2 nucleotide positions, was obtained from a custom RNA synthesis service (Hokkaido System Science). The 5′-phosphorylated last half of pre-tRNA$^{\mathrm{Val}}$ was prepared as follows.

First, a 2 mL in vitro transcription reaction was performed at 42 °C for 2 h in a buffer containing 40 mM Tris-HCl, pH 8.0, 5 mM DTT, 20 mM MgCl$_2$, 1 mM spermidine, 50 μg/mL bovine serum albumin, 2 mM each NTP, 20 mM GMP, 0.1 mg/mL T7 RNA polymerase, and template DNA amplified by 800 μL (16 × 50 μL) PCR with primers, T7_primer; 5′-GGGGCTGCAG TAATACGACT CACTAT-3′ (26 mer) and Aae_Val_CCA_stopOMe; 5′-TG$_{\mathrm{m}}$GTAGGCGC GGGGGGACT-3′ (19 mer; G$_{\mathrm{m}}$: 2′-O-methylguanosine) from pUC_AaValG1. The template containing 2′-O-methylnucleotide is able to reduce nontemplated nucleotide addition by T7 RNA polymerase[73]. After removing the precipitate by centrifugation, the reaction mixture was loaded onto a HiTrap Q HP (1 mL) column (Cytiva). The column was washed with T.35 buffer (20 mM Tris-HCl, pH 7.6, 10 mM MgCl$_2$, and 0.35 M NaCl) to remove unreacted NTPs. The *A. aeolicus* tRNA$^{\mathrm{Val}}$G1A transcript was then eluted with T1.0 buffer (20 mM Tris-HCl, pH 7.6, 10 mM MgCl$_2$, and 1.0 M NaCl) and recovered from the fractions by ethanol precipitation. Typically, 1.5 mg of the tRNA$^{\mathrm{Val}}$G1A transcript was obtained.

Subsequently, 280 μL of approximately 5 mg/mL tRNA$^{\mathrm{Val}}$G1A transcript solution was mixed with 80 μL of 5× annealing buffer (250 mM Tris-HCl, pH 7.6, 500 mM MgCl$_2$), incubated at 65 °C for 5 min, and gradually cooled to 15 °C. The solution of tRNA$^{\mathrm{Val}}$G1A transcript was then placed in ice water, and 40 μL of 2.1 mg/mL RNase T1 was added and mixed. The reaction mixture was incubated at 0 °C for 10 min. RNA fragments were extracted by phenol treatment and recovered by ethanol precipitation. The last half of pre-tRNA$^{\mathrm{Val}}$ was purified by 10% PAGE containing 7 M urea. Typically, 400 μg of the last half of pre-tRNA$^{\mathrm{Val}}$ was obtained.

The 5′-terminus of the purified last half of pre-tRNA$^{\mathrm{Val}}$ was phosphorylated in a 400 μL reaction volume at 37 °C for 30 min in a buffer containing 50 mM Tris-HCl, pH 8.0, 10 mM MgCl$_2$, 5 mM DTT, 1 mM ATP, 2.5 mg/mL of the last half of pre-tRNA$^{\mathrm{Val}}$, and 3 μM T4 polynucleotide kinase. The reaction was stopped by phenol treatment, and the phosphorylated last half of pre-tRNA$^{\mathrm{Val}}$ was recovered by ethanol precipitation.

Finally, we ligated the first half and the 5′-phosphorylated last half of pre-tRNA$^{\mathrm{Val}}$. The reaction mixture (200 μL) without T4 RNA ligase 1 (50 mM HEPES-NaOH, pH 7.4, 15 mM MgCl$_2$, 3.5 mM DTT, 12.5 mg/mL BSA, 4% PEG 6000, 150 μM first half of pre-tRNA$^{\mathrm{Val}}$, 100 μM phosphorylated last half of pre-tRNA$^{\mathrm{Val}}$, and 0.16 mM ATP) was incubated at 65 °C for 5 min, and gradually cooled to 15 °C. T4 RNA ligase 1 was then added at a final concentration of 1 μM, and the reaction mixture was incubated at 37 °C for 30 min. The ligated pre-tRNA$^{\mathrm{Val}}$ was purified by 10% PAGE containing 7 M urea. Approximately 350 μg of the phosphorothioate-modified pre-tRNA$^{\mathrm{Val}}$ was obtained.

Preparation of RNAs for 3′ processing assays

A DNA template for in vitro transcription was amplified by 200 μL (4 × 50 μL) PCR from an appropriate plasmid DNA with an appropriate combination of primers, as follows.

For pre-tRNA$^{\mathrm{Val}}$ carrying a 4-nt 5′-leader and a 30-nt 3′-trailer, Val(4,30), pUC_Aa4Val30 was used as the PCR template with T7_primer and Aae_Val30nt_OMe; 5′-GG$_{\mathrm{m}}$AATTTTTA TTAAGCGCT-3′ (19 mer).

For pre-tRNA$^{\mathrm{Val}}$ lacking 5′-leader and carrying the 30-nt 3′-trailer, Val(0,30), pUC_Aa4Val30 was used as the PCR template with T7_Aae_Val_A1_P; 5′-GGGGCTGCAG TAATACGACT CACTATTAGG CGCGTAGCTC AGTAGGGA-3′ (38 mer) and Aae_Val30nt_OMe.

For tandem pre-tRNA$^{\mathrm{Gly\text{-}Thr}}$ carrying a 12-nt 5′-leader / 32-nt intercistronic region / 30-nt 3′-trailer, Tandem, pUC_Aa12Gly-Thr30 was used as the PCR template with T7_primer and Aae_Thr30nt_OMe; 5′-TG$_{\mathrm{m}}$TAAAGAGG GATTTTTATC-3′ (20 mer).

For pre-tRNA$^{\mathrm{Gly}}$ lacking 5′-leader and carrying the 32-nt 3′-trailer, Gly(0,32), pUC_Aa12Gly-Thr30 was used as the PCR template with T7_Aae_Gly_P; 5′-CGACCTGCAG TAATACGACT CACTATAGCG GGCG TAGCTC AGTTGGTA-3′ (48 mer) and Aae_Gly32nt_OMe; 5′-TU$_{\mathrm{m}}$ATTT ATTG AAGGAAGGGA T-3′ (21 mer; U$_{\mathrm{m}}$: 2′-O-methyluridine).

For pre-tRNA$^{\mathrm{Thr}}$ lacking 5′-leader and carrying the 30-nt 3′-trailer, Thr(0,30), pUC_Aa12Gly-Thr30 was used as the PCR template with T7_Aae_Thr_P; 5′-CGACCTGCAG TAATACGACT CACTATAGCC CAGGTAGCTC AGTCGGTA-3′ (48 mer) and Aae_Thr30nt_OMe.

In vitro transcription reaction (0.5 mL) was performed at 42 °C for 2 h in the buffer described above. When preparing Val(0,30), AMP was used instead of GMP due to the T7 φ2.5 promoter, which enhances the incorporation of adenylate at the transcription start site[74]. The resulting transcripts were purified by 10% PAGE containing 7 M urea.

The RNA 31-mer with the sequence 5′-ACCAUCUUAAUUAGCG CUUAAUAAAAAUUCC-3′ was obtained from a custom RNA synthesis service (Hokkaido System Science).

Cryo-EM sample preparation and data collection of AaHARP and HtHARP

Protein *Aa*HARP or *Ht*HARP (150 μM) in 50 mM Tris-HCl, pH 8.0, 200 mM NaCl, 1 mM TCEP, and 10 mM MgCl$_2$ was mixed with the prepared phosphorothioate-modified *A. aeolicus* pre-tRNA^{Val} (400 μM) in ddH$_2$O. Protein solution and pre-tRNA solution were mixed at a ratio of 1:1, and the mixture was incubated at 4 °C for five days (*Aa*HARP-pre-tRNA) or 20 min (*Ht*HARP-pre-tRNA). For cryo-grid preparation, 3 μL of the sample mixtures were applied onto glow-discharged holey carbon grids (Quantifoil R1.2/1.3 Au200 or Cu300). The grids were blotted and then flash-frozen in liquid ethane using a Vitrobot Mark IV (Thermo Fisher Scientific). For *Aa*HARP-pre-tRNA data collection, micrographs were acquired on a CRYO ARM 300 II (JEOL) microscope equipped with an Omega energy filter, operating at an accelerating voltage of 300 kV. The slit width of the Omega energy filter was set to 20 eV. The movie micrographs (5760 × 4092 pixels) were collected using a K3 direct electron detector (Gatan) at a nominal magnification of 60,000 (0.79 Å/pixel). Fifty movie fractions were recorded at an exposure of 1.1 electrons per Å^2 per fraction. The defocus steps used were − 0.8, − 1.2, − 1.6, and − 2.0 μm. For *Ht*HARP-pre-tRNA data collection, micrographs were acquired on a Titan Krios G4 (Thermo Fisher Scientific) microscope equipped with a Selectris-X energy filter, operating at 300 kV. The slit width of the Selectris-X energy filter was set to 10 eV. The movie micrographs (4096 × 4096 pixels) were collected using a Falcon 4i direct electron detector at a nominal magnification of 215,000 (0.58 Å/pixel). Forty-nine movie fractions were recorded at an exposure of 1.0 electrons per Å^2. The defocus steps used were − 0.8, − 1.2, − 1.6, and − 2.0 μm.

Cryo-EM data processing of *Aa*HARP:pre-tRNA complex

The dataset was processed using RELION-3.1.3[75]. First, the movie fractions were aligned, dose-weighted, and averaged using RELION's implementation[75] on 7 × 5 tiled fractions with a B-factor of 150. The non-weighted movie sums were used for Contrast Transfer Function (CTF) estimation with the CTFFIND-4.1 program[76]. The dose-weighted sums were used for all subsequent steps of image processing. The subsequent processes of particle picking, two-dimensional (2D) classification, ab initio reconstruction, three-dimensional (3D) classification, 3D refinement, CTF refinement, and Bayesian polishing were performed using RELION-3.1.3.

From 2688 micrographs, 1,578,041 picks were Laplacian-of-Gaussian (LoG) selected and extracted while rescaling to 1.58 Å/pixel with a 150-pixel box size. After two cycles of reference-free 2D classification, 400,376 particles corresponding to the best 14 classes, which had approximately 300 Å diameter and displayed secondary-structural elements, were selected and used for ab initio reconstruction (asymmetry, single expected class, 300 Å mask diameter). The generated ab initio map was used as an initial 3D reference for the first 3D classification (4 expected classes, 300 Å mask diameter). After three cycles of 3D classification, 142,831 particles of the best 3D class, which displayed the highest resolution, were used for subsequent 3D refinements (C1 symmetry, 300 Å mask diameter). The refined volume and particle images were rescaled to 0.79 Å/pixel with a 300-pixel box size and used for 3D refinement (C1 symmetry, 300 Å mask diameter). The 3D refinement (C1 symmetry, 300 Å mask diameter) with a soft-edged 3D mask (15-pixel extension, 30-pixel soft cosine edge) was executed after each CTF refinement and Bayesian polishing step. We used this map as a 3D reference for template-matching-based auto-pick by RELION-3.1.3.

From 8362 micrographs, 4,522,335 picks were automatically selected and extracted while rescaling to 2.37 Å/pixel with a 128-pixel box size. The extracted particles were subjected to reference-free 2D classification (100 expected classes, 320 Å mask diameter). The 3,928,948 particles corresponding to the best 5 classes were split into 4 sets. The particles of each set were subjected to 3D classification (3 expected classes, 300 Å mask diameter). A total of 1,404,802 particles from the 4 split sets were used for the subsequent two cycles of 3D classification. The 3D volume and 1,237,200 particles of the best 3D class, which displayed the highest resolution, were used for subsequent 3D refinements. The refined volume and particle images were rescaled to 0.79 Å/pixel with a 384-pixel box size and used for 3D refinement (C1 symmetry, 300 Å mask diameter). The generated 3D refined map was used for the second no-alignment 3D classification (2 expected classes, 320 Å mask diameter). The 3D volume and 578,312 particles of the best 3D class, which displayed the highest resolution, were used for subsequent 3D refinement (C1 symmetry, 300 Å mask diameter). A cycle of CTF refinement and Bayesian polishing was performed. The final 3D refinement (C2 symmetry, 240 Å mask diameter) with a soft-edged 3D mask (15-pixel extension, 30-pixel soft cosine edge) and post-processing generated the final result at 2.87 Å resolution. The 3D FSC analysis showed a sphericity of 0.863.

For the calculation of global resolution estimation after each 3D refinement, the gold-standard Fourier Shell Correlation (FSC) resolution with a criterion of 0.143 was used. The local resolution was estimated using the implementation in RELION-3.1.3. The model-to-map FSC resolution with a 0.5 criterion was calculated using phenix.mtriage[77]. For visualization of the output 3D images, UCSF Chimera[78] was used. The cryo-EM data processing of *Aa*HARP:pre-tRNA complex is summarized in Supplementary Fig. 1 and 2.

Cryo-EM data processing of *Ht*HARP:pre-tRNA complex

The dataset was processed using RELION-4.1[79]. First, the movie fractions were aligned, dose-weighted, and averaged using RELION's implementation[79] on 5 × 5 tiled fractions with a B-factor of 200. The non-weighted movie sums were used for Contrast Transfer Function (CTF) estimation with the Gctf program[80]. The dose-weighted sums were used for all subsequent steps of image processing. The subsequent processes of particle picking, two-dimensional (2D) classification, ab initio reconstruction, three-dimensional (3D) classification, 3D refinement, CTF refinement, and Bayesian polishing were performed using RELION-4.1.

From 2000 micrographs, 273,130 picks were automatically selected by crYOLO[81] and extracted while rescaling to 2.81 Å/pixel with a 128-pixel box size. After two cycles of reference-free 2D classification, 69,507 particles corresponding to the best 89 classes, which had approximately 300 Å diameter and displayed secondary-structural elements, were selected and used for ab initio reconstruction (C1 symmetry, single expected class, 320 Å mask diameter). The generated ab initio map was used as an initial 3D reference for 3D classification (4 expected classes, 320 Å mask diameter). The 3D volume and 28,898 particles of the best 3D class, which displayed the highest resolution, were used for subsequent 3D refinements (C1 symmetry, 320 Å mask diameter).

Among the 273,130 particles, the first 100,000 particles were selected and used for reference-free 2D classification. The 19,056 particles corresponding to the best 10 classes, which had approximately 300 Å diameter and displayed secondary-structural elements, were selected and used as a 2D reference for template-matching-based auto-pick by RELION-4.1. From 11,206 micrographs, 1,861,832 picks were automatically selected and extracted while rescaling to 2.81 Å/pixel with a 128-pixel box size. The extracted particle images were subjected to reference-free 2D classification for two cycles (200 expected classes, 300 Å mask diameter).

After two cycles of reference-free 2D classification, 487,569 particles corresponding to the best 39 classes, which had approximately 300 Å diameter and displayed secondary-structural elements, were selected. The refined volume above was used as a 3D reference for 3D classification (4 expected classes, 320 Å mask diameter). The 3D volume and 191,471 particles of the best 3D class, which displayed the highest resolution, were used for subsequent 3D refinements (C1 symmetry, 320 Å mask diameter). The refined volume and particle images were rescaled to 1.16 Å/pixel with a 320-pixel box size and used for 3D refinement (C1 symmetry, 320 Å mask diameter). The refined volume and particle images were rescaled again to 0.87 Å/pixel with a

400-pixel box size and used for 3D refinement (C1 symmetry, 320 Å mask diameter). The generated 3D refined map and 191,471 particles were subjected to two cycles of CTF refinement and Bayesian polishing. The final 3D refinement (C1 symmetry, 320 Å mask diameter) with a soft-edged 3D mask (15-pixel extension, 30-pixel soft cosine edge) and post-processing generated the final result at 3.19 Å resolution. The 3D FSC analysis showed a sphericity of 0.752.

For the calculation of global resolution estimation after each 3D refinement, the gold-standard Fourier Shell Correlation (FSC) resolution with a criterion of 0.143 was used. The local resolution was estimated using the implementation in RELION-4.1. The model-to-map FSC resolution with a 0.5 criterion was calculated using phenix.mtriage[77]. For visualization of the output 3D images, UCSF Chimera[78] was used. The cryo-EM data processing of *Ht*HARP:pre-tRNA complex is summarized in Supplementary Figs. 3 and 4.

Cryo-EM model building

A model was built manually for cryo-EM reconstructions. As for the model building of the *Aa*HARP dodecamer, the potential maps of the terminal dimers (A1/A2 and F1/F2) were relatively weaker than those for the other dimers. Hence, the terminal A1/A2 and F1/F2 dimers were constructed as poly-Ala models. The building model was improved using a real-space refinement in Phenix[82] combined with iterative rounds of building in COOT[83]. Molprobity[84] and Mtriage[77] were used to evaluate the model. The model statistics are listed in Table S1. Figures and videos were prepared using PyMOL (Schrödinger, LLC) and UCSF Chimera[78].

Fluorescence polarization binding assays

Binding assays were performed in LBS OptiPlate-384 F black polystyrene plates (ParkinElmer). *Aa*HARP wild-type and variants were serially diluted from 5 μM to 10 nM. Enzyme-substrate mixtures were incubated at 23 ± 1 °C in 50 mM Tris-HCl, pH 8.0, 200 mM NaCl, 1 mM TCEP, 20 mM $CaCl_2$, in the presence of 20 nM 5′-fluorescein-labeled *S. cerevisiae* pre-tRNA^{Phe} carrying a 5-nt 5′-leader. The fluorescein-labeled pre-tRNA^{Phe} was obtained from a custom RNA synthesis service (IDT). Polarization readings of the 5′-fluorescein-pre-tRNA tag were measured with a Tecan Ultra plate reader using an excitation wavelength of 485 nm and an emission wavelength of 535 nm. The data were analyzed, and Kd values were calculated via non-linear regression analysis for one-site binding with GraphPad Prism 5.

Pre-tRNA 5′-processing assays

Processing assays were carried out in reaction buffer (20 mM Tris-HCl, pH 8.0, 100 mM NaCl, 1 mM TCEP, and 10 mM $MgCl_2$). Cleavage assays were performed with 0.5 μM *Aa*HARP and 1 μM *A. thaliana* pre-tRNA^{Cys} carrying a 9-nt 5′-leader at 37 °C for 30 min. The reaction solutions were subjected to electrophoresis on 15% TBE-urea gels. The gels were stained with SYBR Gold (Thermo Fisher Scientific). The pre-tRNA substrate and the 5′-matured product were visualized at 412 nm using a transilluminator.

Pre-tRNA 3′-processing assays

Processing assays were carried out in 20 mM Tris-HCl, pH 8.0, 100 mM NaCl, 1 mM TCEP, 10 mM $MgCl_2$, 0.5 μ/μl RNase inhibitor (Nippon Gene), in the presence of 2 μM *Aa*HARP (wild-type or variants) or *Ht*HARP, and 5 μM pre-tRNAs (*A. aeolicus* pre-tRNA^{Val} carrying a 4-nt 5′-leader / 30-nt 3′-trailer [Val(4,30)], *A. aeolicus* pre-tRNA^{Val} carrying a 30-nt 3′-trailer [Val(0,30)], *A. aeolicus* tandem pre-tRNA$^{Gly\text{-}Thr}$ carrying a 12-nt 5′-leader / 32-nt intercistronic region / 30-nt 3′-trailer [Tandem], *A. aeolicus* pre-tRNA^{Gly} carrying a 32-nt 3′-trailer [Gly(0,32)], and *A. aeolicus* pre-tRNA^{Thr} carrying a 30-nt 3′-trailer [Tyr(0,30)]). Reaction mixtures were incubated at 37 °C for 30 min. The reaction solutions were subjected to 10% PAGE containing 7 M urea. The gels were stained with Toluidine Blue O (MERCK).

Mass spectrometry analysis of HARP cleavage products

To analyze the pre-tRNA cleavage products produced by *Aa*HARP, the respective pre-tRNA (5 μM; [Val(4,30)] or [Thr(0,30)]) was incubated in the presence of 20 mM Tris-HCl, pH 8.0, 100 mM NaCl, 1 mM TCEP, 10 mM $MgCl_2$, 0.5 U/μl RNase inhibitor, and 2 μM *Aa*HARP at 37 °C for 30 min. An aliquot (5 μl) was mixed with 200 μl of 1 M NH_4Cl, and the mixture was loaded on a small C18 column containing 10 μl of ODS-AQ-HG resin (YMC Co., Ltd.) equilibrated with 10 mM triethylammonium bicarbonate (TEAB), pH 7.0. The column was washed twice with 200 μl of 10 mM TEAB (pH7.0), and the adsorbed RNA was eluted with 50 μl acetonitrile. The eluate was dried, and the RNA was dissolved in 3 μl water. An aliquot (1 μl) of the sample was mixed with 1 μl of MALDI matrix (20 mg/ml 3-hydroxypicolinic acid and 5 mg/ml diammonium hydrogen citrate in 45% acetonitrile and 0.045% trifluoroacetic acid) and the mixture was spotted onto a MALDI plate. Mass spectrometry acquisitions of the RNA on the plate were carried out on an Axima Resonance™ MALDI-QIT-TOF mass spectrometer system under Launchpad 2.9.1 and Shimadzu Biotech MALDI-MS software. Laser power was optimized for each sample between 140 and 160, profiles were 500 per sample, 2 shots were accumulated per sample, and acquisition was conducted in positive mode. RNase T1 digested RNA fragments from the yeast tRNAPhe transcript were used for external calibration. The Mass spectrometry data were analyzed using mMass v5.5.0. Each data was acquired from a single replicate ($n = 1$).

Protein preparation and pre-tRNA processing assay of *Aa*Rng

The cDNA sequences encoding *Aa*Rng (residues 2–458) was subcloned into the pE_SUMO vector, which encodes an N-terminal His_6-SUMO tag. The cDNA sequence is listed in Supplementary Table 2. Recombinant *Aa*Rng was expressed in the *E. coli* strain BL21-CodonPlus (DE3)-RIL (Agilent Technologies). The proteins were first purified by Ni-NTA agarose chromatography (Fujifilm Wako Chemicals), and the eluted proteins were subsequently digested by Ulp1 to remove the SUMO-tag, followed by purification on a HiLoad 16/60 Superdex 200 column (Cytiva) equilibrated with 50 mM Tris-HCl, pH 8.0, 200 mM NaCl, 0.5 mM TCEP. The peak fractions containing the target proteins were pooled and concentrated to 10–20 mg/mL. Processing assays were carried out using the same procedure as for *Aa*HARP.

Reporting summary

Further information on research design is available in the Nature Portfolio Reporting Summary linked to this article.

Data availability

The cryo-EM maps of *Aa*HARP:pre-tRNA and *Ht*HARP:pre-tRNA were deposited in the Electron Microscopy Data Bank under accession codes EMD-37128 and EMD-37129, respectively. Structural coordinates were deposited at the Protein Data Bank under accession codes 8KD9 and 8KDA, respectively. Source data are provided in this paper.

References

1. Abbott, J. A., Francklyn, C. S. & Robey-Bond, S. M. Transfer RNA and human disease. *Front. Genet.* **5**, https://doi.org/10.3389/fgene.2014.00158 (2014).
2. Schaffer, A. E., Pinkard, O. & Coller, J. M. TRNA Metabolism and Neurodevelopmental Disorders. *Annu. Rev. Genom. Hum. Genet.* **20**, 359–387 (2019).
3. Kirchner, S. & Ignatova, Z. Emerging roles of tRNA in adaptive translation, signalling dynamics and disease. *Nat. Rev. Genet.* **16**, 98–112 (2015).
4. Giegé, R. et al. Structure of transfer RNAs: Similarity and variability. *Wiley Interdiscip. Rev. RNA* **3**, 37–61 (2012).
5. Biela, A. et al. The diverse structural modes of tRNA binding and recognition. *J. Biol. Chem.* **299**, 104966 (2023).

6. Hartmann, R. K., Gößringer, M., Späth, B., Fischer, S. & Marchfelder, A. Chapter 8 The Making of tRNAs and More - RNase P and tRNase Z. *Pro. Mol. Biol. Transl. Sci.* **85**, 319–368 (2009).
7. Ruiz-Arroyo, V. M. et al. Structures and mechanisms of tRNA methylation by METTL1–WDR4. *Nature* **613**, 383–390 (2023).
8. Li, J. et al. Structural basis of regulated m7G tRNA modification by METTL1–WDR4. *Nature* **613**, 391–397 (2023).
9. Ohira, T. et al. Reversible RNA phosphorylation stabilizes tRNA for cellular thermotolerance. *Nature* **605**, 372–379 (2022).
10. Esakova, O. A. et al. Structural basis for tRNA methylthiolation by the radical SAM enzyme MiaB. *Nature* **597**, 566–570 (2021).
11. Ohira, T. & Suzuki, T. Transfer RNA modifications and cellular thermotolerance. *Mol. Cell* **84**, 94–106 (2024).
12. Wang, Y. et al. tRNA modifications: insights into their role in human cancers. *Trends Cell Biol.* **33**, 1035–1048 (2023).
13. Phizicky, E. M. & Hopper, A. K. The life and times of a tRNA. *RNA* **29**, 898–957 (2023).
14. Hayne, C. K. et al. Structural basis for pre-tRNA recognition and processing by the human tRNA splicing endonuclease complex. *Nat. Struct. Mol. Biol.* **30**, 824–833 (2023).
15. Sekulovski, S., Sušac, L., Stelzl, L. S., Tampé, R. & Trowitzsch, S. Structural basis of substrate recognition by human tRNA splicing endonuclease TSEN. *Nat. Struct. Mol. Biol.* **30**, 834–840 (2023).
16. Zhang, X. et al. Structural basis of pre-tRNA intron removal by human tRNA splicing endonuclease. *Mol. Cell***83**, 1328–1339 (2023).
17. Phizicky, E. M. & Hopper, A. K. tRNA biology charges to the front. *Genes Dev.* **24**, 1832–1860 (2010).
18. Sekulovski, S. & Trowitzsch, S. Transfer RNA processing-from a structural and disease perspective. *Biol. Chem.* **403**, 749–763 (2022).
19. Phan, H. D., Lai, L. B., Zahurancik, W. J. & Gopalan, V. The many faces of RNA-based RNase P, an RNA-world relic. *Trends Biochem. Sci.* **46**, 976–991 (2021).
20. Bhatta, A. & Hillen, H. S. Structural and mechanistic basis of RNA processing by protein-only ribonuclease P enzymes. *Trends Biochem. Sci.* **47**, 965–977 (2022).
21. Wu, J. et al. Cryo-EM Structure of the Human Ribonuclease P Holoenzyme. *Cell* **175**, 1393–1404.e11 (2018).
22. Reiter, N. J. et al. Structure of a bacterial ribonuclease P holoenzyme in complex with tRNA. *Nature* **468**, 784–791 (2010).
23. Lan, P. et al. Structural insight into precursor tRNA processing by yeast ribonuclease P. *Science* **362**, https://doi.org/10.1126/science.aat6678 (2018).
24. Wan, F. et al. Cryo-electron microscopy structure of an archaeal ribonuclease P holoenzyme. *Nature Communications* **10**, 2617 (2019).
25. Guerrier-Takada, C., Gardiner, K., Marsh, T., Pace, N. & Altman, S. The RNA moiety of ribonuclease P is the catalytic subunit of the enzyme. *Cell* **35**, 849–857 (1983).
26. Zhu, J. et al. Structural and mechanistic basis for recognition of alternative tRNA precursor substrates by bacterial ribonuclease P. *Nat. Commun.* **13**, 1–13 (2022).
27. Warnecke, J. M., Fürste, J. P., Hardt, W. D., Erdmann, V. A. & Hartmann, R. K. Ribonuclease P (RNase P) RNA is converted to a Cd2+-ribozyme by a single Rp-phosphorothioate modification in the precursor tRNA at the RNase P cleavage site. *Proc. Natl. Acad. Sci. USA* **93**, 8924–8928 (1996).
28. Warnecke, J. M., Green, C. J. & Hartmann, R. K. Role of metal ions in the cleavage mechanism by the e. colirnase p holoenzyme. *Nucleosides Nucleotides* **16**, 721–725 (1997).
29. Pfeiffer, T. et al. Effects of phosphorothioate modifications on precursor tRNA processing by eukaryotic RNase P enzymes. *J. Mol. Biol.* **298**, 559–65 (2000).
30. Chen, Y., Li, X. & Gegenheimer, P. Ribonuclease P catalysis requires Mg2+ coordinated to the pro-R(P) oxygen of the scissile bond. *Biochemistry* **36**, 2425–2438 (1997).
31. Mann, H., Ben-Asouli, Y., Schein, A., Moussa, S. & Jarrous, N. Eukaryotic RNase P: Role of RNA and protein subunits of a primordial catalytic ribonucleoprotein in RNA-based catalysis. *Mol. Cell* **12**, 925–35 (2003).
32. Buck, A. H., Kazantsev, A. V., Dalby, A. B. & Pace, N. R. Structural perspective on the activation of RNase P RNA by protein. *Nat. Struct. Mol. Biol.y* **12**, 958–964 (2005).
33. Kazantsev, A. V. & Pace, N. R. Bacterial RNase P: A new view of an ancient enzyme. *Nat. Rev. Microbiol.* **4**, 729–740 (2006).
34. Holzmann, J. et al. RNase P without RNA: identification and functional reconstitution of the human mitochondrial tRNA processing enzyme. *Cell* **135**, 462–474 (2008).
35. Gobert, A. et al. A single Arabidopsis organellar protein has RNase P activity. *Nat. Struct. Mol. Biol.* **17**, 740–744 (2010).
36. Nickel, A. I. et al. Minimal and RNA-free RNase P in Aquifex aeolicus. *Proc. Natl. Acad. Sci. USA* **114**, 11121–11126 (2017).
37. Lechner, M. et al. Distribution of ribonucleoprotein and protein-only RNase P in Eukarya. *Mol. Biol. Evol.* **32**, 3186–3193 (2015).
38. Taschner, A. et al. Nuclear RNase P of Trypanosoma brucei: A Single Protein in Place of the Multicomponent RNA-Protein Complex. *Cell Reports* **2**, 19–25 (2012).
39. Teramoto, T. et al. Minimal protein-only RNase P structure reveals insights into tRNA precursor recognition and catalysis. *J. Biol. Chem.* **297**, https://doi.org/10.1016/j.jbc.2021.101028 (2021).
40. Feyh, R. et al. Structure and mechanistic features of the prokaryotic minimal rnase p. *ELife* **10**, https://doi.org/10.7554/elife.70160 (2021).
41. Howard, M. J., Lim, W. H., Fierke, C. A. & Koutmos, M. Mitochondrial ribonuclease P structure provides insight into the evolution of catalytic strategies for precursor-tRNA 5′ processing. *Proc. Natl. Acad. Sci. USA* **109**, 16149–16154 (2012).
42. Gobert, A. et al. Structural insights into protein-only RNase P complexed with tRNA. *Nat. Commun.* **4**, https://doi.org/10.1038/ncomms2358 (2013).
43. Reinhard, L., Sridhara, S. & Hällberg, B. M. Structure of the nuclease subunit of human mitochondrial RNase P. *Nucleic Acids Res.* **43**, 5664–5672 (2015).
44. Li, F., Liu, X., Zhou, W., Yang, X. & Shen, Y. Auto-inhibitory mechanism of the human mitochondrial RNase P protein complex. *Sci. Rep.* **5**, https://doi.org/10.1038/srep09878 (2015).
45. Karasik, A., Shanmuganathan, A., Howard, M. J., Fierke, C. A. & Koutmos, M. Nuclear Protein-Only Ribonuclease P2 Structure and Biochemical Characterization Provide Insight into the Conserved Properties of tRNA 5′ End Processing Enzymes. *J. Mol. Biol.* **428**, 26–40 (2016).
46. Pinker, F. et al. Biophysical analysis of Arabidopsis protein-only RNase P alone and in complex with tRNA provides a refined model of tRNA binding. *J. Biol. Chem.* **292**, 13904–13913 (2017).
47. Bhatta, A., Dienemann, C., Cramer, P. & Hillen, H. S. Structural basis of RNA processing by human mitochondrial RNase P. *Nat. Struct. Mol. Biol.* **28**, 713–723 (2021).
48. Wu Meyers, N., Karasik, A., Kaitany, K., Fierke, C. A. & Koutmos, M. Gambogic acid and juglone inhibit RNase P through distinct mechanisms. *J. Biol. Chem.* **298**, 102683 (2022).
49. Gößringer, M., Wäber, N. B., Wiegard, J. C. & Hartmann, R. K. Characterization of RNA-based and protein-only RNases P from bacteria encoding both enzyme types. *RNA* **29**, 376–391 (2023).
50. Li, Y. et al. Crystal structures and insights into precursor tRNA 5′-end processing by prokaryotic minimal protein-only RNase P. *Nat. Commun.* **13**, 2290 (2022).

51. Walczyk, D. et al. Analysis of the cleavage mechanism by protein-only RNase P using precursor tRNA substrates with modifications at the cleavage site. *J. Mol. Biol.* **428**, 4917–4928 (2016).
52. Kaberdin, V. R. & Bizebard, T. Characterization of Aquifex aeolicus RNase E/G. *Biochem. Biophys. Res. Commun.* **327**, 382–392 (2005).
53. Willkomm, D. K., Feltens, R. & Hartmann, R. K. tRNA maturation in Aquifex aeolicus. *Biochimie* **84**, 713–722 (2002).
54. Zhang, J. & Ferré-D'Amaré, A. R. Trying on tRNA for size: RNase P and the T-box riboswitch as molecular rulers. *Biomolecules* **6**, https://doi.org/10.3390/biom6020018 (2016).
55. Redko, Y., Li de laSierra-Gallay, I. & Condon, C. When all's zed and done: The structure and function of RNase Z in prokaryotes. *Nat. Rev. Microbiol.* **5**, 278–286 (2007).
56. Li, Z., Gong, X., Joshi, V. H. & Li, M. Co-evolution of tRNA 3′ trailer sequences with 3′ processing enzymes in bacteria. *RNA* **11**, (2005).
57. Shepherd, J. & Ibba, M. Bacterial transfer RNAs. *FEMS Microbiol. Rev.* **39**, 280–300 (2015).
58. Tomita, K. & Welner, A. M. Collaboration between CC- and A-adding enzymes to build and repair the 3′-terminal CCA of tRNA in Aquifex aeolicus. *Science* **294**, https://doi.org/10.1126/science.1063816 (2001).
59. Tomita, K. et al. Structural basis for template-independent RNA polymerization. *Nature* **430**, 700–704 (2004).
60. Lombo, T. B. & Kaberdin, V. R. RNA processing in Aquifex aeolicus involves RNase E/G and an RNase P-like activity. *Biochem. Biophys. Res. Commun.* **366**, 457–463 (2008).
61. Ishii, R., Nureki, O. & Yokoyama, S. Crystal structure of the tRNA processing enzyme RNase PH from Aquifex aeolicus. *J. Biol. Chem.* **278**, 32397–32404 (2003).
62. Minagawa, A., Takaku, H., Takagi, M. & Nashimoto, M. A novel endonucleolytic mechanism to generate the CCA 3′ termini of tRNA molecules in Thermotoga maritima. *J. Biol. Chem.* **279**, 15688–15697 (2004).
63. ten Broeke-Smits, N. J. P. et al. Operon structure of Staphylococcus aureus. *Nucleic Acids Res.* **38**, 3263–3274 (2010).
64. Dar, D. & Sorek, R. High-resolution RNA 3-ends mapping of bacterial Rho-dependent transcripts. *Nucleic Acids Res.* **46**, 6797–6805 (2018).
65. Li, Z. & Deutscher, M. P. RNase E plays an essential role in the maturation of Escherichia coli tRNA precursors. *RNA* **8**, 97–109 (2002).
66. Ow, M. C. & Kushner, S. R. Initiation of tRNA maturation by RNase E is essential for cell viability in E. coli. *Genes and Dev.* **16**, 1102–1115 (2002).
67. Mohanty, B. K., Petree, J. R. & Kushner, S. R. Endonucleolytic cleavages by RNase e generate the mature 3′ termini of the three proline tRNAs in Escherichia coli. *Nucleic Acids Res.* **44**, 6350–6362 (2016).
68. Régnier, P. & Grunberg-Manago, M. Cleavage by RNase III in the transcripts of the metY-nusA-infB operon of Escherichia coli releases the tRNA and initiates the decay of the downstream mRNA. *J. Mol. Biol.* **210**, 293–302 (1989).
69. Dutta, T., Malhotra, A. & Deutscher, M. P. Exoribonuclease and endoribonuclease activities of RNase BN/RNase Z both function in vivo. *J. Biol. Chem.* **287**, 35747–35755 (2012).
70. Dutta, T. & Deutscher, M. P. Catalytic properties of RNase BN/RNase Z from Escherichia coli. RNase BN is both an exo- and endoribonuclease. *J. Biol. Chem.* **284**, 15425–15431 (2009).
71. Taniguchi, N., Nakayama, S., Kawakami, T. & Murakami, H. Patch cloning method for multiple site-directed and saturation mutagenesis. *BMC Biotechnol.* **13**, https://doi.org/10.1186/1472-6750-13-91 (2013).
72. Yokogawa, T. et al. Identification of a radical SAM enzyme involved in the synthesis of archaeosine. *Nat. Chem. Biol.* **15**, 1148–1155 (2019).
73. Kao, C., Zheng, M. & Rüdisser, S. A simple and efficient method to reduce nontemplated nucleotide addition at the 3′ terminus of RNAs transcribed by T7 RNA polymerase. *RNA* **5**, 1268–1272 (1999).
74. Huang, F., Bugg, C. W. & Yarus, M. RNA-catalyzed CoA, NAD, and FAD synthesis from phosphopantetheine, NMN, and FMN. *Biochemistry* **39**, 15548–15555 (2000).
75. Zivanov, J. et al. New tools for automated high-resolution cryo-EM structure determination in RELION-3. *ELife* **7**, https://doi.org/10.7554/elife.42166 (2018).
76. Rohou, A. & Grigorieff, N. CTFFIND4: Fast and accurate defocus estimation from electron micrographs. *J. Struct. Biol.* **192**, 216–221 (2015).
77. Afonine, P. V. et al. New tools for the analysis and validation of cryo-EM maps and atomic models. *Acta Crystallogr. Sect. D Struct. Biol.* **74**, 814–840 (2018).
78. Pettersen, E. F. et al. UCSF Chimera - A visualization system for exploratory research and analysis. *J. Comput. Chem.* **25**, 1605–1612 (2004).
79. Kimanius, D., Dong, L., Sharov, G., Nakane, T. & Scheres, S. H. W. New tools for automated cryo-EM single-particle analysis in RELION-4.0. *Biochem. J.* **478**, 4169–4185 (2021).
80. Zhang, K. Gctf: Real-time CTF determination and correction. *J. Struct. Biol.* **193**, 1–12 (2016).
81. Wagner, T. et al. SPHIRE-crYOLO is a fast and accurate fully automated particle picker for cryo-EM. *Commun. Biol.* **2**, https://doi.org/10.1038/s42003-019-0437-z (2019).
82. Liebschner, D. et al. Macromolecular structure determination using X-rays, neutrons and electrons: Recent developments in Phenix. *Acta Crystallogr. Sect. D Struct. Biol.* **75**, 861–877 (2019).
83. Emsley, P. & Cowtan, K. Coot: Model-building tools for molecular graphics. *Acta Crystallogr. Sect. D Biol. Crystallogr.* **60**, 2126–2132 (2004).
84. Chen, V. B. et al. MolProbity: All-atom structure validation for macromolecular crystallography. *Acta Crystallogr. Sect. D Biol. Crystallogr.* **66**, 12–21 (2010).

Acknowledgements

We are grateful to Prof. Makoto Kimura for guidance in this work. We thank Tomoyuki Numata for providing experimental materials and guidance in this work. We thank Masato Kawasaki and Akihito Ikeda for assisting with the cryo- EM data collection and Toshio Moriya for having a discussion on the cryo-EM single particle analysis. We thank Tomohito Tanihara, Yuma Terada, Kaita Otsuki, Yuya Yoshida, Naoya Matsunaga and Shigehiro Ohdo of Structural Drug Discovery Center via Green-Pharma at Pharmaceutical Sciences Kyushu University for their technical support for using CRYO ARM300 II (JP22ama121031: S. Ohdo). We would like to thank Editage (www.editage.jp) for English language editing. We thank the Center for Advanced Instrumental and Educational Support of the Faculty of Agriculture (Kyushu University) for technical support. This work was supported by Grant-in-aid for scientific research by JSPS KAKENHI (grant number 21K06032:T.T., 24K09353:Y.K.) and the Platform Project for Supporting Drug Discovery and Life Science Research (Basis for Supporting Innovative Drug Discovery and Life Science Research [BINDS]) from the Japan Agency for Medical Research and Development (AMED) (grant number JP21am0101071:T.S. and JP21am0101091:K.M.) (supporting no. 3051).

Author contributions

T.T. and Y.K. conceived the project. T.T. and T.K. performed recombinant protein purification and ternary complex reconstitution. T.T., T.K., T.Y., K.M., and N.A. prepared and optimized samples for cryo-EM. T.T., T.K., K.M., and N.A. performed cryo-EM data processing. T.T. built models. T.T., T.K., and T.Y. performed biochemical experiments. T.N., T.S., and Y.K. supervised the project. All authors organized and analyzed the data. T.T., T.K. and Y.K. wrote the manuscript with input from all authors.

Competing interests

The authors declare no competing interests.

Additional information

Supplementary information The online version contains supplementary material available at https://doi.org/10.1038/s41467-025-60002-1.

Correspondence and requests for materials should be addressed to Takamasa Teramoto or Yoshimitsu Kakuta.

Peer review information *Nature Communications* thanks Sebastian Glatt, Roland Hartmann, Andrés Palencia, and the other anonymous reviewer(s) for their contribution to the peer review of this work. A peer review file is available.

Reprints and permissions information is available at http://www.nature.com/reprints

Publisher's note Springer Nature remains neutral with regard to jurisdictional claims in published maps and institutional affiliations.

Open Access This article is licensed under a Creative Commons Attribution-NonCommercial-NoDerivatives 4.0 International License, which permits any non-commercial use, sharing, distribution and reproduction in any medium or format, as long as you give appropriate credit to the original author(s) and the source, provide a link to the Creative Commons licence, and indicate if you modified the licensed material. You do not have permission under this licence to share adapted material derived from this article or parts of it. The images or other third party material in this article are included in the article's Creative Commons licence, unless indicated otherwise in a credit line to the material. If material is not included in the article's Creative Commons licence and your intended use is not permitted by statutory regulation or exceeds the permitted use, you will need to obtain permission directly from the copyright holder. To view a copy of this licence, visit http://creativecommons.org/licenses/by-nc-nd/4.0/.

© The Author(s) 2025